TRENDS IN SCIENCES 2026; 23(9): 13225
https://doi.org/10.48048/tis.2026.13225 RESEARCH ARTICLE

# Improved Nitrate Adsorption by Thai Perlite: A Comprehensive Study of Equilibrium, Kinetics, Thermodynamics, and Mechanisms for Sustainable Water Treatment Aligned with SDGs

**Suchada Sawasdee*and Prachart Watcharabundit**

*Department of Chemistry, Faculty of Science and Technology, Thepsatri Rajabhat University, Lopburi 15000, Thailand*

**(*Corresponding author's e-mail: suchada.s@lawasri.tru.ac.th)**

*Received: 31 December 2025, Revised: 31 January 2026, Accepted: 7 February 2026, Published: 1 April 2026*

**Abstract**

Nitrate contamination in agricultural groundwater poses significant environmental and health risks. Developing low-cost, locally available adsorbents is crucial for sustainable water treatment. Raw perlite (RP) and acid-modified perlite (MP) were investigated as adsorbents for nitrate removal in batch systems. Both perlites were characterized via nitrogen adsorption-desorption, Fourier transform infrared spectroscopy, X-ray fluorescence spectroscopy, X-ray diffraction spectroscopy, and scanning electron microscopy. Adsorption performance was evaluated under varying pH, contact time, and initial nitrate concentration conditions. Equilibrium data were analyzed using the Langmuir, Freundlich, and Dubinin-Radushkevich isotherm models, while kinetic and thermodynamic parameters were assessed to elucidate the adsorption mechanism. HCl modification enhanced the structural and surface properties of perlite. Optimal adsorption occurred at pH 6 with an equilibrium time of 60 min. The Langmuir model best described the equilibrium data, with maximum adsorption capacities of 39.22 mg/g for RP and 54.94 mg/g for MP at 30 °C. Kinetic analysis indicated a pseudo-second-order model fit, and thermodynamic evaluation confirmed that the adsorption process was endothermic and spontaneous. Mechanistic insights revealed that physical adsorption predominated, driven mainly by electrostatic interaction, hydrogen bonding, electrostatic displacement, cation bridging, pore filling, and ion exchange. Regeneration tests demonstrated good reusability of both adsorbents for up to 5 cycles. HCl-modified perlite exhibits superior adsorption capacity and reusability compared to raw perlite. These findings highlight its potential as an efficient and sustainable adsorbent for nitrate removal from groundwater. Furthermore, this research significantly contributes to the United Nations Sustainable Development Goals (SDGs), specifically SDG 6 (Target 6.3) by enhancing water quality and SDG 12 (Targets 12.4 & 12.5) through the valorization of local mineral resources and the promotion of circular economy principles.

**Keywords:** Adsorption, Mechanism, Perlite, Nitrate, Groundwater

## Introduction

The growing number of agricultural activities, necessary for enhancing food production and industrial operations, is the primary factor behind the rising levels of nitrate pollution in groundwater [1] and surface water, due to the high solubility of nitrate in water [2]. Nitrate has been identified as a crucial and indispensable nutrient for the growth of plants and algae [3]. The use of an excessive quantity of fertilizer is encouraged in agriculture. Fertilizers and agrochemicals have contaminated agricultural water supplies. The excessive use of nitrogen fertilizers and poor management of industrial waste can lead to eutrophication, characterized by high nitrate levels that promote the overgrowth of plants and algae in water [4]. Additionally, drinking water with a nitrate concentration over 10 ppm is dangerous, as high levels of nitrogen compounds can lead to health problems like alimentary canal cancer and cyanosis in children [5,6]. Excessive

nitrate consumption can reduce blood hemoglobin, impairing oxygen transport. High nitrate levels in drinking water can also lead to the formation of carcinogenic nitrosamines and increase the risk of infant methemoglobinemia, or blue-baby syndrome [7,8]. Growing demands for better water quality and safety in developing nations require the implementation of nitrate remediation systems [3]. The WHO's maximum contaminant level (MCL) for nitrate in drinking water is 50 mg/L as nitrate, while the US Environmental Protection Agency (USEPA) sets the limit for nitrate-nitrogen ($NO_3^-N$) at 10 mg/L [9,10].

Nitrate is difficult to remove by conventional water treatment methods because of its high solubility and chemical stability [1]. Ion exchange, reverse osmosis, adsorption, chemical, and biological methods have all been used to remove nitrate from water [11]. Ion exchange and adsorption are the most widely used and efficient methods for removing nitrates from water. Adsorption is particularly favored for its cost-effectiveness and low risk of creating further contamination [12]. While activated carbon is a highly effective adsorbent due to its large surface area, its high cost and reliance on coal—a finite resource—are significant drawbacks [13]. Alternative adsorbents have recently been developed due to their abundance and low cost. Recently, there has been a growing interest in using inexpensive industrial and agricultural waste as an adsorbent to treat wastewater [14]. Several other materials, including corn stalks [10], ceramic waste [15], and steel slag [14], have been employed as adsorbents to eliminate nitrate. With this in mind, various adsorbents have been tested for the removal of nitrate and other pollutants from water, such as clay, chitosan, zeolite, carbon-based adsorbents, and agro-industrial waste materials. Perlite, commonly regarded as a rhyolitic glass, consists of more than 70% silica and approximately 13% alumina [4]. The tetrahedral coordination between silicon and oxygen atoms is retained at the surface of perlite glass. Under ambient conditions, these sites bond with monovalent hydroxyl groups to complete their coordination, thereby forming silanol and silanediol groups [16]. The silanol groups, together with alumina hydrous oxide groups on the perlite surface, can effectively attract and immobilize a wide range of contaminants, including heavy metals, organic compounds, and other hazardous substances [17]. Malakootian *et al.* [18] demonstrated the application of perlite for the removal of lead (Pb) and cadmium (Cd) from paint industry effluents. Likewise, Selengil and Yildiz [19] reported that expanded perlite exhibited a notable adsorption capacity for methylene blue in aqueous solutions.

Adsorbent materials can be modified chemically and physically using different techniques. Chemical modification of the surface is beneficial for adsorbents as it directly alters the material's surface chemistry. Chemical processes employ acids, alkalis, or salts to enhance the surface functional groups. The key mechanism driving efficient nitrate removal is the enhanced positive surface charges of the adsorbents, which also create new surface functional groups with a more effective affinity for nitrate. Acid alters the chemical composition of adsorbents, resulting in an augmentation of the density of positively charged particles on their surfaces. According to Loganathan *et al.* [20], electrostatic attraction will induce a high concentration of positive charges to adsorb additional negatively charged nitrate anions. The interactions between the nitrate ion and the adsorbent, which move it from the aqueous solution to the adsorbent surface, provide the basis for nitrate removal by adsorption. Changing the adsorbent's structure makes it possible to attain the primary objective of the adsorption process, which is to have an adsorbent with a high adsorption capacity and high selectivity for the nitrate ion. Various techniques have been employed to alter the surface of adsorbents to enhance their ability to retain nitrates. These techniques include protonation (treatment with acid), grafting groups (such as carboxyl, hydroxyl, or amine), impregnation with metal or metal oxide, and modification of surfactants [21].

This study investigated a novel adsorbent derived from HCl-modified volcanic rock perlite for nitrate removal. Batch experiments were conducted to evaluate the effects of key parameters, including pH, contact time, initial nitrate concentration, and temperature. The physical and chemical properties of the adsorbent were comprehensively characterized using FTIR, XRD, BET, XRF, and SEM analyses. Nitrate removal behavior was further examined through kinetic, thermodynamic, equilibrium, and mechanistic modeling. In addition, the adsorbent's reusability was assessed, and its practical applicability was demonstrated using real agricultural

groundwater. Beyond its scientific contributions, this research advances global sustainability goals by addressing SDG 6 (Target 6.3: Water quality improvement) and SDG 12 (Targets 12.4 and 12.5: Sustainable resource management and waste reduction), thereby underscoring the potential of low-cost, geo-sourced materials in circular water treatment solutions.

## Materials and methods

### Materials

Sodium nitrate ($NaNO_3$), brucine sulphate, sulphanilic acid, sulphuric acid, sodium hydroxide, hydrochloric acid, sodium carbonate, and sodium phosphate were obtained from Merck (Germany). All reagents employed in this study were of analytical grade. Distilled water was used throughout for the preparation of solutions.

### Preparation of adsorbents and an adsorbate

The raw perlite (RP) was obtained in its natural form from the Sa Bot District, Lopburi Province, Thailand. After being thoroughly rinsed with distilled water, the samples were dried in a hot air oven at 100 °C. The dried perlite powder was then immersed in a 0.1 M hydrochloric acid solution for 24 h at ambient temperature. The modified perlite (MP) was subsequently washed with distilled water until a neutral pH was achieved and dried again at 100 °C. After being sieved to obtain a particle size of 50 - 100 mesh, the dried perlite and bentonite were stored in a desiccator for future use.

A nitrate stock solution (1,000 mg/L) was prepared by dissolving 1.371 g of sodium nitrate in distilled water. Before making up the volume to 1 L, 20 mL of 1.0 M HCl was added to suppress interference from hydroxide and carbonate ions, and the solution was stored for use. The absorbance of the standards and the residual nitrate concentration in the samples were determined colorimetrically using a UV-visible spectrophotometer (Analytik Jena, Specord 210 plus, Germany) with the brucine method at 410 nm [22].

### Characterization of adsorbents

Several analytical techniques were employed to characterize the adsorbents. XRF (HORIBA MESA-500W, Japan) was used to determine elemental composition, while XRD (Rigaku SmartLab2, Japan) was applied to analyze the crystalline structure. Surface morphology was examined using SEM (LEO 1450 VP, Leo, UK), and FTIR (Perkin Elmer Model Two, USA) was used to identify surface functional groups. The BET surface area was obtained from $N_2$ adsorption-desorption isotherms measured using a Quantachrome Autosorb 1 MP gas sorption analyzer (USA).

### Batch experiments of adsorption

The adsorption experiments were carried out in 250-mL flasks containing 0.3 g of adsorbent and 100 mL of nitrate solution. Experimental conditions were varied to evaluate the effects of pH (2 - 12), contact time (1 - 240 min), initial nitrate concentration (25 - 300 mg/L), and temperature (20 - 40 °C). Each flask containing the nitrate-adsorbent suspension was agitated at 200 rpm. At predetermined time intervals, the solid adsorbent was separated by filtration, and the residual nitrate concentration in the filtrate was quantified using a UV-visible spectrophotometer at 410 nm. This quantification relied on the reaction of nitrate with brucine sulfate in 13 N sulfuric acid, which produces a yellow-colored complex detectable at the specified wavelength (410 nm). The adsorption capacity (mg/g) and percentage removal (%) were subsequently calculated according to Eqs. (1) and (2), respectively.

$$q_t = \frac{(C_o - C_t)V}{W} \quad (1)$$

$$\% \text{ adsorption} = \frac{(C_o - C_t)\times 100}{C_o} \quad (2)$$

where, $C_o$ (mg/L) is the initial concentration, $C_t$ (mg/L) is the concentration at any given time, $q_t$ (mg/g) is the quantity adsorbed at any given time, V(L) is the volume of the solution, and W(g) is the adsorbents' mass.

### Adsorption isotherm

The distribution of molecules between the liquid and solid phases at equilibrium during the adsorption process appears clearer in the adsorption isotherm. The Langmuir, Freundlich, and Dubinin-Radushkevich isotherms were used in this investigation to assess the

adsorption data. Eq. (3) present linear equations for the Langmuir isotherm [3].

$$\frac{C_e}{q_e}=\frac{1}{q_{max}}C_e+\frac{1}{K_L q_{max}} \quad (3)$$

where, $C_e$ (mg/L) is the equilibrium concentration, $q_e$ (mg/g) is the amount adsorbed at equilibrium, $K_L$ is the Langmuir constant, and $q_{max}$ (m/g) is the maximum adsorption capacity. A dimensionless separation factor can be used to describe the fundamental properties of the Langmuir isotherm. ($R_L$) which is defined by Eq. (4).

$$R_L = \frac{1}{(1+K_L C_o)} \quad (4)$$

Eq. (5) present linear equations for the Freundlich isotherm [3].

$$\log\ q_e = \log\ K_F + (1/n)\log\ C_e \quad (5)$$

where, $K_F$ (L/g) is the adsorption capacity, and the adsorption intensity is represented by 1/n.

Eq. (6) present linear equations for the Dubinin-Radushkevich isotherm.

$$\ln\ q_e = \ln\ q_o - K_{DR}[RT \ln (1+1/C_e)]^2 \quad (6)$$

where, $q_e$ (mg/g) signifies the quantity of nitrate adsorbed per gram of adsorbent at equilibrium; $q_0$ (mg/g) indicates the maximum adsorption capacity; R is the gas constant (L·atm/(mol·K)), and T represents the absolute temperature in Kelvin (K). $K_{DR}$ (mol²/kJ²) is obtained from the slope of the linear graph depicting ln $q_e$ against $[RT \ln (1 + 1/C_e)]^2$. The $K_{DR}$ indicates the average adsorption energy (E, kJ/mol) of the adsorbate, as expressed by Eq. (7).

$$E = \frac{1}{\sqrt{2K_{DR}}} \quad (7)$$

The adsorption energy (E) below 8 kJ/mol is generally indicative of physisorption. When E lies within the range of 8 - 16 kJ/mol, the adsorption process can be classified as chemisorption [23].

**The kinetic models**

Investigating adsorption kinetics can provide important novel insights into the adsorption mechanism. The kinetic experiment examines an adsorbate's ability to adsorb onto an adsorbent throughout a range of time intervals. The adsorption data are analyzed in this study using the pseudo-first-order, pseudo-second-order, and intraparticle diffusion models. The linear representations of the pseudo-first-order, pseudo-second-order, and intraparticle diffusion models are given by Eqs. (8) - (10), respectively [3].

$$\log (q_e - q_t) = \log\ q_e - \frac{k_1}{2.303}t \quad (8)$$

$$\frac{t}{q_t}=\frac{1}{k_2 q_e^2}+\frac{1}{q_e}t \quad (9)$$

$$q_t = K_{id}(t)^{1/2} + C \quad (10)$$

where, $k_1$ (1/min) and $k_2$ (g/mg·min) are the pseudo-first-order and pseudo-second-order models' respective rate constants. The $q_t$ (mg/g) and $q_e$ (mg/g) are the equilibrium time and the amounts adsorbed at any time (min), respectively. The intraparticle diffusion rate constant is denoted by $K_{id}$ (mg/g.min$^{1/2}$), and C is the intercept.

**Kinetic validation**

Simply estimating the normalized standard deviation, $\Delta q_e$ (%), using Eq. (11), one may determine which model more accurately depicts the adsorption process [24].

$$\Delta q_e\ (\%) = 100\times\sqrt{\frac{[(q_{t,exp} - q_{t,cal})/q_{t,exp}]^2}{N-1}} \quad (11)$$

where, N is the number of data points, $q_{t,exp}$(mg/g) is the experimental adsorption capacity. For the pseudo-first and pseudo-second models, $q_{t,cal}$ (mg/g) represents the computed adsorption capacity.

**Thermodynamic parameter of adsorption**

Utilizing examination of the adsorption of the adsorbate onto the surface of the adsorbent, the thermodynamic behavior is evaluated to understand the changes in Gibbs energy (ΔG), enthalpy (ΔH), and entropy (ΔS). Eq. (12) can be used to express the Gibbs free energy change (ΔG) throughout the adsorption process.

$$\Delta G = -RT \ln K_c \quad (12)$$

where $K_c$ ($K_c = q_e/C_e$) is the equilibrium constant, R is the gas constant, and T is the absolute temperature. Eq. (13) can also be used to determine changes in enthalpy (ΔH) and entropy (ΔS).

$$\ln K_c = \frac{\Delta S}{R} - \frac{\Delta H}{RT} \quad (13)$$

The slope and intercept from the linear plot between $\ln K_c$ and 1/T can be utilized for calculating ΔH and ΔS, respectively.

## Results and discussion

**XRF analysis**

X-ray fluorescence (XRF) analysis revealed that the primary elements in both RP and MP adsorbents, before and after adsorption, were Si, K, Fe, and Al (Table 1). Specifically, RP contained Si (64.154%), K (23.180%), Fe (6.387%), and Al (4.551%), while MP exhibited a highly similar composition: Si (63.585%), K (23.060%), Fe (6.720%), and Al (4.621%). After nitrate adsorption, the percentages of Si (63.821%), K (22.741%), and Al (4.162%) in RP and Si (62.854%), K (22.307%), and Al (4.323%) in MP decreased. The reduction in Al and K levels suggests that nitrate adsorption on the adsorbent surface is influenced by cation exchange [25]. Si/Al ratio showed 14.09 and 13.78 for RP and MP, respectively. The content of Al increased from 4.55% in RP to 4.61% in MP; therefore, MP can adsorb a larger amount of nitrate, due to the amphoteric properties of $Al_2O_3$. However, Yang *et al.* [14] reported that the surface of $Al_2O_3$ is not only suitable for nitrate adsorption but also exhibits affinity toward most oxyanions.

**Table 1** Chemical composition of adsorbents before and after nitrate adsorption.

| RP | | | | MP | | | |
|---|---|---|---|---|---|---|---|
| **before adsorption** | | **after adsorption** | | **before adsorption** | | **after adsorption** | |
| **elements** | **unit (%)** | **elements** | **unit (%)** | **elements** | **unit (%)** | **elements** | **unit (%)** |
| Si | 64.154 | Si | 63.821 | Si | 63.585 | Si | 62.854 |
| K | 23.180 | K | 22.741 | K | 23.060 | K | 22.307 |
| Fe | 6.387 | Fe | 7.134 | Fe | 6.720 | Fe | 7.837 |
| Al | 4.551 | Al | 4.152 | Al | 4.612 | Al | 4.323 |

**Nitrogen adsorption-desorption isotherm**

The nitrogen adsorption-desorption isotherms and pore size distributions of RP and MP are presented in **Figure 1**, while the BET surface area, pore volume, average pore radius, and pore diameter are summarized in **Table 2**. According to the nitrogen adsorption-desorption isotherms shown in **Figures 1(a**) and **1(b)**, both RP and MP are identified as predominantly mesoporous materials, exhibiting the characteristic Type IV isotherm with average pore diameters in the range of 2 - 50 nm [26]. **Figures 1 (c)** and **1(d)** show the BJH pore size distribution, with the median pore sizes of RP and MP calculated as 4.06 and 3.61 nm, respectively. The BET specific surface areas were 23.08 $m^2/g$ for RP and 15.69 $m^2/g$ for MP. The average pore diameter was calculated using the relation $D_p = \frac{4V \times 1000}{\text{BET surface area}}$. The pore volume and pore diameter were 0.0487 cc/g and 8.44 nm for RP, and 0.035 cc/g and 8.92 nm for MP, respectively. The total pore volume of RP at 0.999 $P/P_0$ was 31.47 cc/g, whereas that of MP at 0.995 $P/P_0$ was 22.63 cc/g. The reduction in BET surface area is likely attributable to the coverage and partial collapse of the internal pore structure during acidification [27]. Comparable reductions in surface area and pore volume, resulting from pore damage and occlusion, have also

been reported following treatment with hydrochloric acid [27] and nitric acid [28].

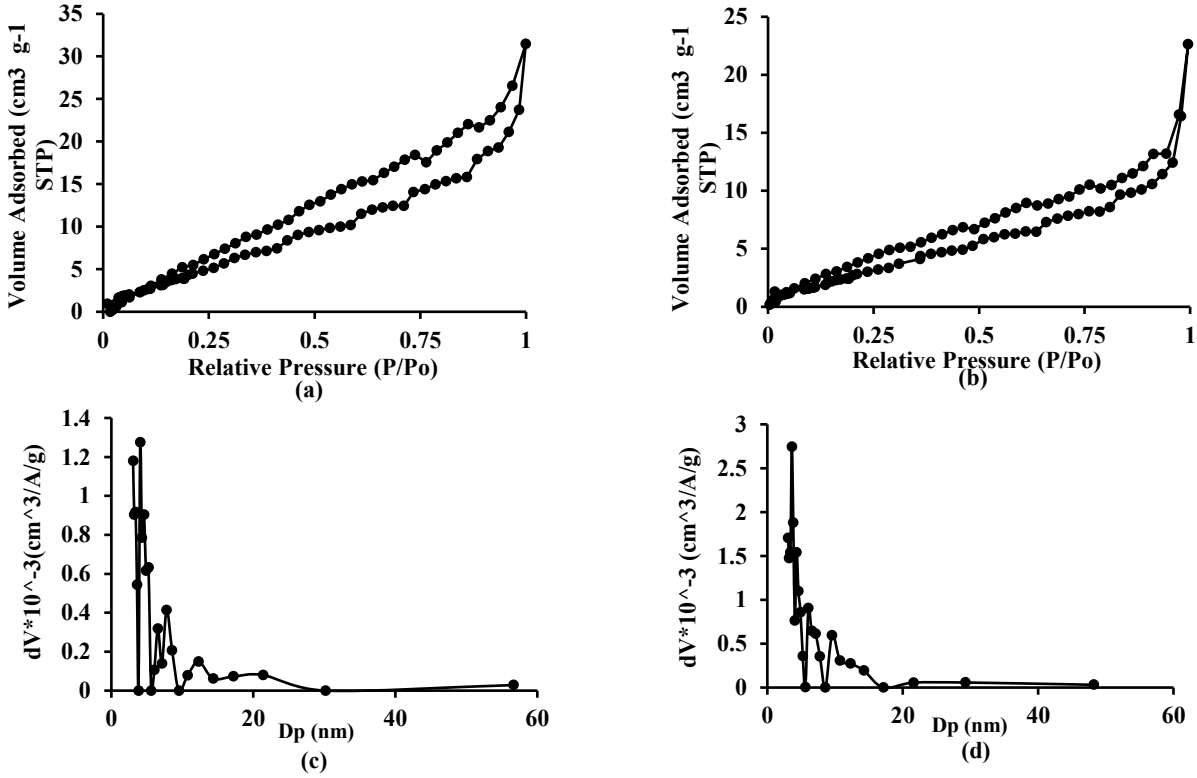


**Figure 1** The plots of nitrogen adsorption-desorption and pore size distribution of RP (a), (c) and of MP (b), (d).

**Table 2** Textural properties of the adsorbents obtained from BET and BJH analyses.

| Parameters | adsorbents | |
|---|---|---|
| | RP | MP |
| BET surface area ($m^2$/g) | 23.08 | 15.69 |
| pore volume (cc/g) | 0.0487 | 0.0350 |
| BET pore diameter (nm) | 8.44 | 8.92 |
| BJH median pore diameter (nm) | 4.06 | 3.61 |

**SEM analysis**

**Figure 2** presents the surface morphology of RP and MP adsorbents before nitrate adsorption. The RP sample (**Figure 2(a)**) exhibits a highly porous framework with irregular, interconnected pores, which explains its relatively higher BET surface area and greater accessibility for nitrate ions. In contrast, the MP sample (**Figure 2(b)**) exhibits a smoother surface with fractured, layered domains, reflecting structural modifications induced by acid treatment. The disappearance of the small pores observed in RP results in a reduction of the BET surface area and pore volume, consistent with the morphological changes seen in MP.

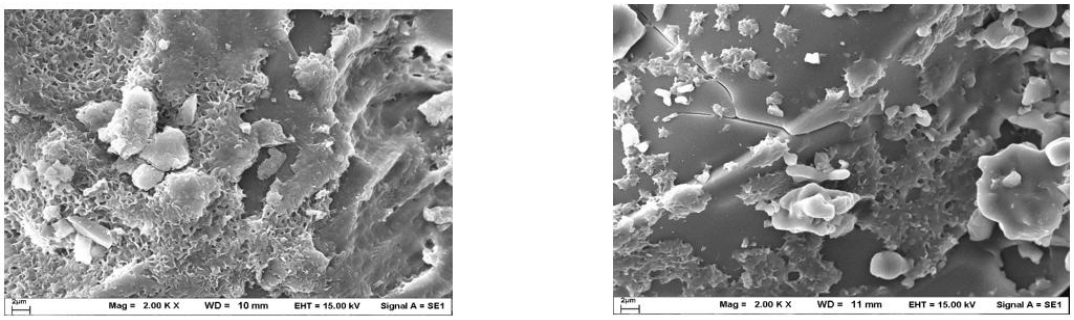


**Figure 2** SEM micrographs of (a) RP and (b) MP before nitrate adsorption, recorded at 2.00 kX magnification.

**XRD analysis**

The XRD patterns of RP and MP before adsorption are shown in **Figure 3**, exhibiting broad amorphous peaks around 2θ ≈ 25°, which confirm the amorphous nature of perlite [29]. Consistent with this observation, Somkiattiyot *et al.* [30] reported large peaks at 2θ = 20° - 62° and 22° - 32°, corresponding to amorphous structural regions. Furthermore, certain amorphous silica phases can transform into crystalline structures, indicating that the removal of specific contaminants increases the relative amount of silica [31]. RP exhibited diffraction peaks at 2θ (°) values of 13.76, 21.90, 22.83, 23.66, 26.52, 27.33, 27.69, 27.96, 29.39, 30.29, 30.94, 35.53, 41.18, 44.90, 46.61, 48.74, 50.90, 54.78, 56.94, 60.36, 64.48, 67.38, 68.40, 74.26, and 74.45, with an average crystallite size of 101.43 nm. In comparison, MP displayed diffraction peaks at 2θ (°) values of 13.59, 13.89, 20.82, 21.88, 23.68, 24.31, 26.62, 27.40, 27.70, 27.98, 30.46, 30.96, 34.21, 35.73, 39.43, 41.11, 41.64, 42.11, 42.51, 50.12, 51.06, 51.31, 56.59, 57.01, 57.25, 60.11, and 61.81, with an average crystallite size of 154.52 nm.

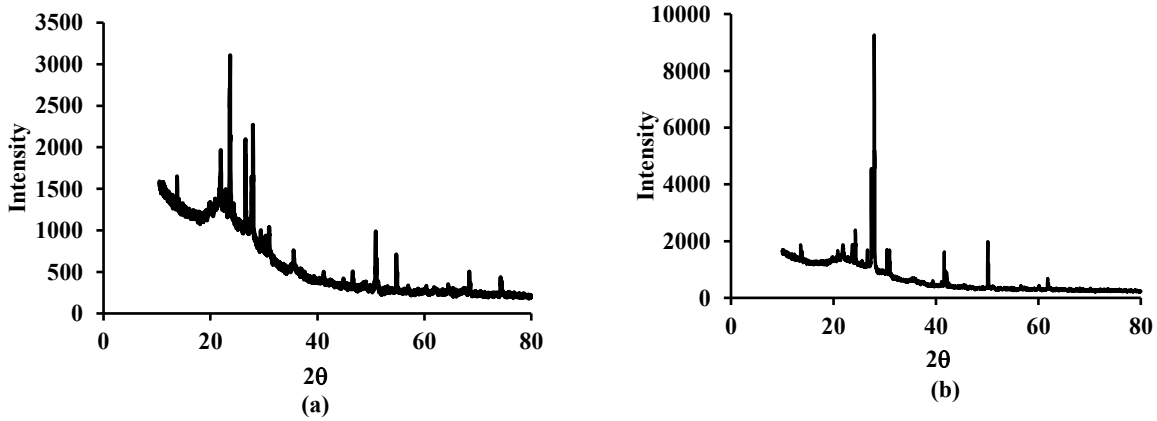


**Figure 3** XRD patterns of (a) RP and (b) MP before nitrate adsorption.

**FTIR analysis**

The FTIR spectra of RP and MP presented in **Figure 4** revealed comparable bands across both adsorbents. The broad band in the range of 3,000 - 3,800 $cm^{-1}$ was assigned to the stretching vibrations of OH groups in different environments [32]. Structural OH stretching vibrations of Si–OH and Al–OH groups were identified as the source of the bands at 3,560 - 3,630 $cm^{-1}$ [33]. The band at 3,739 $cm^{-1}$ corresponds to the contribution of free terminal Si–OH groups. Perlite exhibited a band at 3,622 - 3,640 $cm^{-1}$, which is associated with the stretching vibration of the structural hydroxyl group of Al [32]. Additionally, MP displayed a peak at 3,629 $cm^{-1}$, attributed to Al–OH, whereas this peak was not observed in RP. Peaks between 1,600 - 1,650 $cm^{-1}$ were attributed to bending vibrations of OH groups originating from water molecules [34]. The band at approximately 1,000 $cm^{-1}$ corresponded to stretching vibrations in Si–O–M (M = Al or Si) groups, while symmetric and asymmetric Si–O stretching bands were

observed with similar values. The bands at 750 - 790 $cm^{-1}$ reflected the Si–O bond stretching of silicate structures [33].

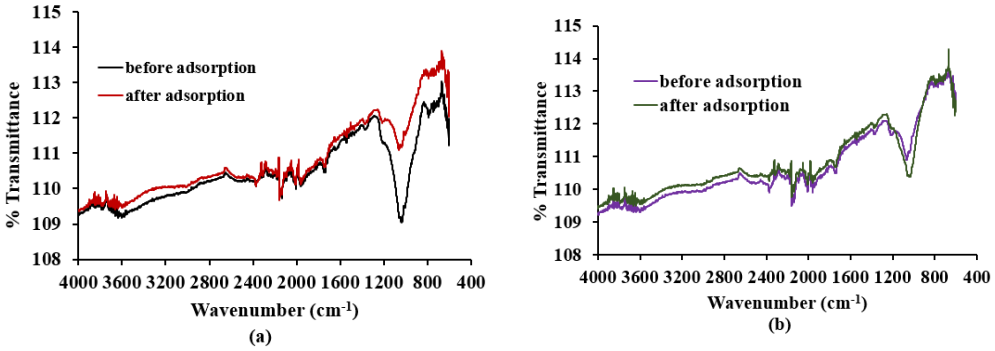


**Figure 4** FTIR spectra of (a) RP and (b) MP before and after nitrate adsorption.

FTIR analysis confirmed distinct spectral changes in RP after nitrate adsorption, indicating the involvement of various surface functional groups in the binding process. A notable increase in peak intensity was observed at 2,374 and 2,006 $cm^{-1}$. Moreover, the initial characteristic peaks at 3,739, 3,600, 2,155, 1,740, 1,369, 1,039, and 791 $cm^{-1}$ shifted to 3,738, 3,638, 3,630, 3,593, 2,157, 1,751, 1,372, 1,061, and 790 $cm^{-1}$, respectively, with new peaks emerging at 3,638 and 3,630 $cm^{-1}$. This behavior indicates that nitrate adsorption occurred at Al–OH groups present on RP. Similarly, the MP adsorbent exhibited structural modifications after nitrate adsorption, as evidenced by the shifting of its characteristic peaks from 2,372, 2,157, 1,736, 1,371, and 1,085 $cm^{-1}$ to 2,375, 2,155, 1,752, 1,368, and 1,032 $cm^{-1}$, respectively. In addition, the MP spectra exhibited new peak intensities at 3,621, 3,735, and 3,739 $cm^{-1}$ after adsorption, confirming that nitrate was adsorbed at Al–OH and Si–OH groups, respectively.

**Effect of pH and pHpzc**

The pH of a solution is a crucial factor influencing adsorption, and the pHpzc (**Figure 4(a)**) defines the specific pH at which the adsorbent surface carries zero net charge. The difference in pHpzc values between RP (6.0) and MP (5.1) provides insight into their adsorption behavior toward nitrate ions. At solution pH values below the pHpzc, the adsorbent surface tends to be positively charged, thereby favoring the electrostatic attraction of negatively charged nitrate ions. Notably, MP achieved higher adsorption efficiency than RP (**Figure 5(b)**) despite its lower BET surface area, suggesting that acid treatment not only reduced pore volume but also modified surface chemistry in a way that enhanced nitrate binding. This modification may have increased the density of Al–OH and Si–OH groups or altered the surface charge, rather than affecting the physical porosity. These findings highlight that adsorption efficiency is governed not only by morphological features but also by the interplay between surface charge characteristics and chemical modifications induced by pretreatment.

As pH increased from 2 to 6 (**Figure 5(b)**), the removal efficiency for RP rose from 77.33% to 85.45%, and for MP from 81.19% to 91.56%. Although adsorption is generally expected to be enhanced at lower pH, due to the positively charged adsorbent surface attracting nitrate anions (Eqs. (14) and (15)), the experimental results demonstrated the opposite trend: The adsorption percentage decreased under more acidic conditions (pH < 6). The observed trend was consistent with nitrate adsorption from aqueous solution using magnetic Mg/Fe hydrotalcite [43] and modified steel slag [14]. This outcome was likely attributable to the compression of the electrical double layer (EDL) and proton-dominated interfacial saturation [44], which,

$$Si–OH + H^+ \rightarrow Si–OH_2^+ \quad (14)$$

$$Si–OH_2^+ + NO_3^- \rightarrow Si–OH_2^+NO_3^- \quad (15)$$

consequently hindered the diffusion and effective approach of nitrate ions to the adsorbent surface, thereby diminishing the efficiency of electrostatic interactions. In addition, the use of HCl for pH adjustment introduced a high concentration of $Cl^-$ ions at low pH. The presence of $Cl^-$ significantly reduced nitrate adsorption on the adsorbent due to competition for active sites [7,14,35], most likely via weak anion exchange or ionic shielding near the active sites [45]. According to Zhu *et al.* [46], the presence of Al increases the effective proton-reactive sites on the adsorbent's crystal face, thereby enhancing its positive surface charge density. This increased surface positivity, as reasoned in the present study, facilitates the electrostatic attraction of nitrate ions. For pH values between 2 and 6, the percentage of adsorption increased with rising solution pH. This behavior can be attributed either to the displacement of chloride ions by nitrate ions or to the reduction of the electrical double layer (EDL) resulting from the decreased $H^+$ concentration. The positively charged surface of the adsorbent would be linked to chloride ions for the hydrochloric acid surface modification, and these ions would then be exchanged for nitrate anions [36], as represented in Eq. (16). Consequently, the adsorption capacity did not attain its maximum under highly acidic conditions (pH < 6), with the highest nitrate removal observed at pH 6.


(16)

An increase in pH from 7 to 12 resulted in a slight decrease in nitrate clearance, from 86.74% to 84.15% for RP and from 90.48% to 90.15% for MP. Although the removal efficiency remained high, this reduction can be attributed to electrostatic repulsion, as negatively charged surfaces repel negatively charged nitrate ions. Comparable findings have been reported for nitrate adsorption on triamine-$SiO_2$ material [37] and nano-alumina [38]. One plausible mechanism is cation bridging, in which divalent cations (e.g., $Ca^{2+}$, $Mg^{2+}$) coordinate simultaneously with negatively charged surface sites and nitrate. This process effectively reduces the electrostatic barrier by forming ternary surface complexes (Si-O$^-$ $Ca^{2+}$...$NO_3^-$), thereby sustaining adsorption even at elevated pH levels. Although direct evidence for nitrate-specific cation bridging is limited, similar mechanisms have been documented in other adsorption systems [47,48]. By analogy, such bridging may also occur between divalent cations and nitrate. This interpretation aligns with the broader framework of surface complexation theory, in which electrostatic interactions and ion coordination jointly govern adsorption behavior.

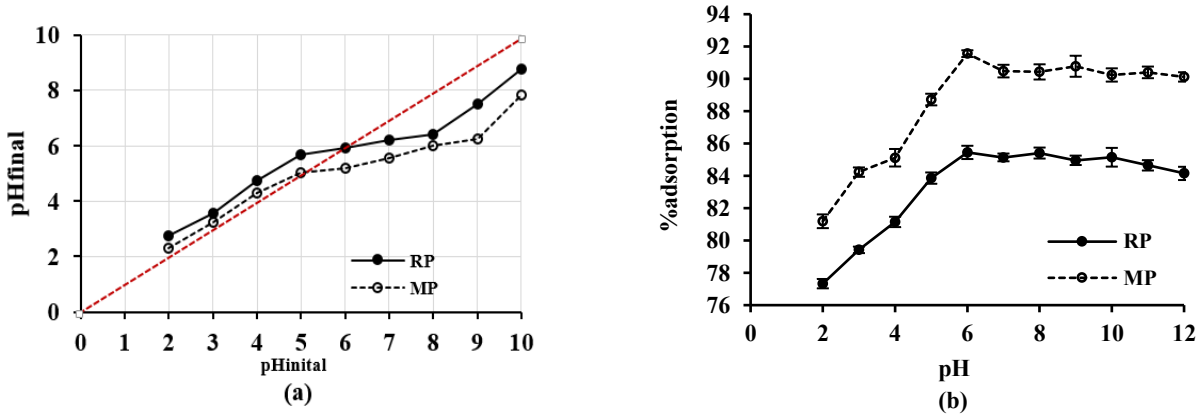


**Figure 5** (a) Determination of the point of zero charge (pHpzc) for RP and MP. (b) Effect of solution pH on adsorption capacity; pH 2–12, contact time 60 min, initial nitrate concentration 50 mg/L, adsorbent dose 0.3 g).

**Effect of contact time and temperatures**

**Figure 6** illustrates the relationship between nitrate adsorption capacity and contact time (1 - 240 min). Adsorption on both RP and MP was rapid within the first 15 min, owing to the abundance of vacant sites and the high initial nitrate concentration. With increasing contact time, adsorption capacity progressively rose as these sites became occupied, but the rate slowed until equilibrium was reached at 60 min. According to Khatamian *et al.* [39], several phenomena

may contribute to the decline in removal efficiency: progressive saturation of active sites by nitrate ions, reduced diffusion from the bulk solution to the adsorbent surface due to concentration gradients, and temporal changes in adsorbate-adsorbent interactions, all of which collectively diminish overall effectiveness. Furthermore, adsorption capacity increased with temperature (**Figure 6**); at equilibrium, RP exhibited capacities of 14.11, 14.58, and 15.32 mg/g, while MP showed 15.31, 15.45, and 15.85 mg/g at 20, 30, and 40 °C, respectively. This indicates that the adsorption process is endothermic. Jiang *et al.* [40] suggested that elevated temperatures enhance particle mobility, thereby increasing the likelihood of adsorbate molecules interacting with functional groups on the adsorbent surface and, consequently, boosting the adsorption capacity.

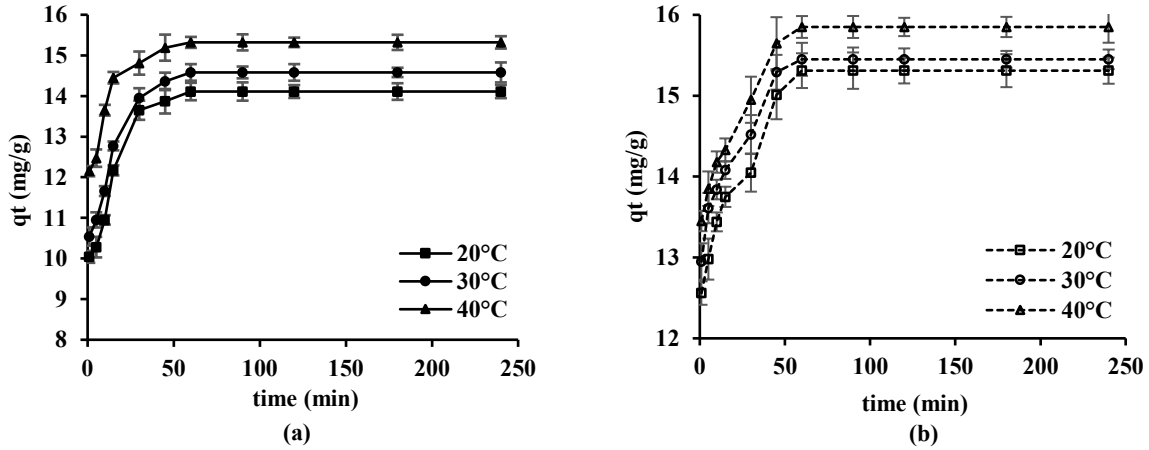


**Figure 6** Plots showing the effect of contact time and temperature on nitrate adsorption for (a) RP and (b) MP; pH 6, contact time 60 min, initial nitrate concentration of 50 mg/L, and adsorbent dose 0.3 g.

**Kinetics and activation energy**

To investigate adsorption kinetics and activation energy, contact-time and temperature-dependent adsorption studies were performed. The nitrate adsorption data, obtained at an initial concentration of 50 mg/L, were analyzed using the linear pseudo-first-order, pseudo-second-order, and intraparticle diffusion models. **Figure 7** presents the plots of three kinetic models, with their corresponding parameter values summarized in **Table 3**. The pseudo-second-order model yielded the highest regression coefficient ($R^2$), reaching 0.999 at 3 distinct temperatures. Moreover, the adsorption capacity ($q_{cal}$) obtained from this model exhibited the closest agreement with the experimental values ($q_{exp}$). Additionally, the pseudo-second-order model showed low error values $\Delta q_e$ (%) of less than 1. The calculated equilibrium capacity ($q_{cal}$) from this model consistently matched the experimental data ($q_{exp}$). This superior fit indicates that the adsorption rate is governed by a chemisorption mechanism, involving the sharing or exchange of electrons between the adsorbent and adsorbate [41]. The adsorption reactions likely proceed through complexation, chelation, and valence forces [42]. A similar observation has been reported for nitrate adsorption by modified corn stalks [10].

As shown in **Figure 7**, the intraparticle diffusion plots of RP exhibited three distinct stages, whereas those of MP displayed two stages. However, none of the plots passed through the origin, indicating that intraparticle diffusion was not the sole rate-limiting step in adsorption onto either adsorbent. This deviation implies that other processes, such as film diffusion or surface adsorption, also contributed to the overall rate of nitrate uptake. Additionally, the liquid film diffusion plots (not shown) were obtained by plotting ln(1–F), where $F = q_t/q_e$, against t. The resulting plots provided slope ($-K_{LF}$) and $R^2$ values, which are summarized in **Table 3**. Based on these $R^2$ values, intraparticle diffusion exhibited a slightly better correlation, although the liquid film diffusion model remains applicable. The coexistence of multiple diffusion pathways highlights the complexity of the adsorption mechanism, with intraparticle diffusion playing a significant role in conjunction with boundary layer effects. These findings are consistent

with previous studies [10,15], which emphasize that adsorption kinetics often involve a combination of external mass transfer and intraparticle diffusion rather than a single controlling mechanism.

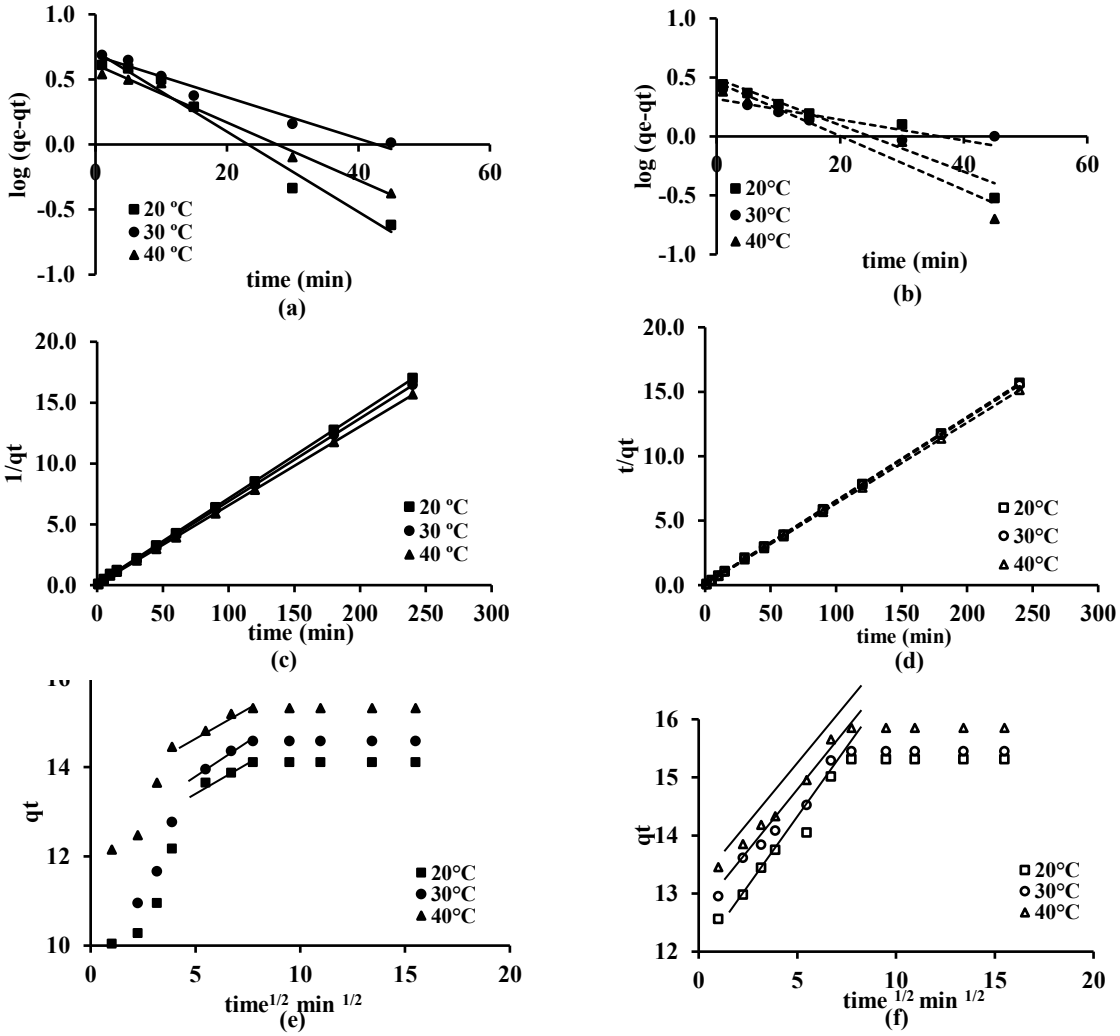


**Figure 7** Plots of kinetic and diffusion models of nitrate adsorption: (a, b) pseudo-first-order; (c, d) pseudo-second-order; (e, f) intraparticle diffusion. RP corresponds to (a, c, e) and MP to (b, d, f); pH 6, contact time 60 min, initial nitrate concentration of 50 mg/L, and adsorbent dose 0.3 g.

**Table 3** Kinetic parameters obtained from nitrate adsorption experiments onto RP and MP at various temperatures (20, 30, and 40 °C).

| Kinetic models | RP | | | MP | | |
|---|---|---|---|---|---|---|
| | **20 °C** | **30 °C** | **40 °C** | **20 °C** | **30 °C** | **40 °C** |
| $q_e$ (exp) (mg/g) | 14.111 | 14.580 | 15.321 | 15.310 | 15.450 | 15.851 |
| **Pseudo-first order** | | | | | | |
| $q_e$ (cal) (mg/g) | 5.191 | 4.806 | 4.105 | 2.997 | 2.875 | 3.063 |
| $k_1$ (1/min) | 0.071 | 0.037 | 0.051 | 0.056 | 0.055 | 0.070 |
| $\Delta q_e$ (%) | 44.689 | 47.588 | 51.977 | 56.427 | 60.174 | 57.841 |

| Kinetic models | RP | | | MP | | |
|---|---|---|---|---|---|---|
| | **20 °C** | **30 °C** | **40 °C** | **20 °C** | **30 °C** | **40 °C** |
| $R^2$ | 0.975 | 0.968 | 0.983 | 0.884 | 0.901 | 0.831 |
| **Pseudo-second order** | | | | | | |
| $q_e$ (cal) (mg/g) | 14.222 | 14.681 | 15.401 | 15.385 | 15.504 | 15.924 |
| $k_2$ (g/(mg·min)) | 0.047 | 0.054 | 0.060 | 0.071 | 0.073 | 0.076 |
| $\Delta q_e$ (%) | 0.556 | 0.489 | 0.369 | 0.345 | 0.247 | 0.326 |
| $R^2$ | 0.999 | 0.999 | 0.999 | 0.999 | 0.999 | 0.999 |
| **Intraparticle diffusion** | | | | | | |
| $K_{id}$ (mg/g·min$^{1/2}$) | 0.202 | 0.279 | 0.227 | 0.409 | 0.367 | 0.369 |
| C (mg/g) | 12.440 | 12.535 | 13.596 | 12.104 | 12.664 | 13.015 |
| $R^2$ | 0.994 | 0.985 | 0.949 | 0.980 | 0.984 | 0.989 |
| **Liquid film diffusion** | | | | | | |
| $K_{LF}$ (1/min) | 0.071 | 0.069 | 0.095 | 0.045 | 1.145 | 1.097 |
| $R^2$ | 0.974 | 0.993 | 0.958 | 0.903 | 0.863 | 0.899 |

In this study, the rate constant ($k_2$) obtained from the pseudo-second-order kinetic model at different temperatures (293, 303 and 313 K) was used to determine the activation energy ($E_a$). A plot of ln $k_2$ versus 1/T (not shown) was constructed, and $E_a$ was calculated from the slope. The calculated $E_a$ values for RP and MP were 9.946 and 2.750 kJ/mol, respectively. According to the activation energy criterion, adsorption can be classified as physisorption when $E_a$ is less than 40 kJ/mol and as chemisorption when $E_a$ exceeds 40 kJ/mol [43]. Therefore, nitrate adsorption on RP and MP was identified as a physisorption process. Consistent with this criterion, Wang *et al.* [10]; Wagner *et al.* [49] reported that nitrate adsorption on magnetic Mg/Fe hydrotalcite and on modified corn stalks also proceeded via physisorption.

**Effect of initial nitrate concentration and adsorption isotherm**

Adsorption experiments were performed at initial nitrate concentrations ranging from 25 to 300 mg/L. As the concentration increased stepwise (25, 50, 100, 200 and 300 mg/L), the adsorption capacity of RP rose from 7.37 to 37.28 mg/g, while that of MP increased from 7.87 to 52.20 mg/g. The experimental plots illustrating the relationship between equilibrium concentration ($C_e$) and adsorption capacity ($q_e$) are presented in **Figure 8**. Consistent with the findings of Elemile *et al.* [3], the adsorption capacity increased with higher initial concentrations, suggesting an enhanced driving force to overcome mass transfer resistances between the liquid and solid phases. Comparable trends have been reported for nitrate adsorption using modified wheat straw [50], modified grape seeds [51], and modified hazelnut shells [13].

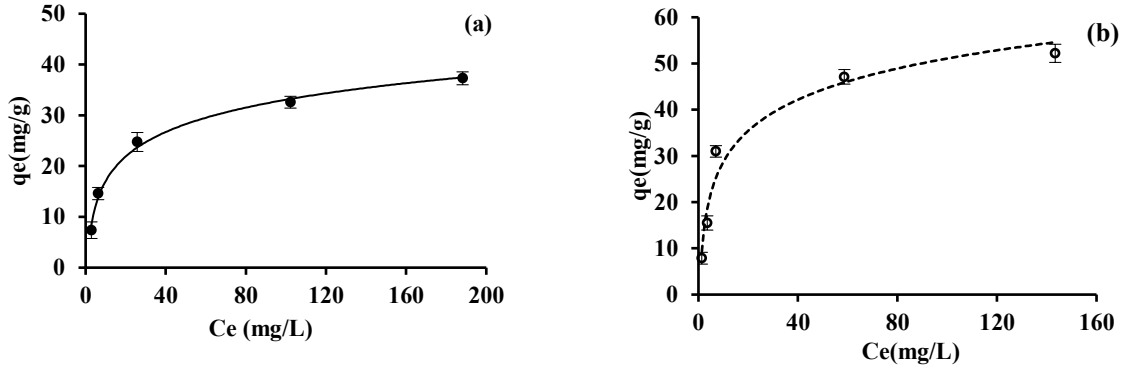


**Figure 8** Effect of initial nitrate concentration on equilibrium adsorption plots for (a) RP and (b) MP; pH 6, contact time 60 min, initial nitrate concentration of 50 mg/L, and adsorbent dose 0.3 g.

The equilibrium adsorption data were analyzed using the linear forms of the Langmuir, Freundlich, and Dubinin-Radushkevich isotherms (**Table 4**). The results clearly indicated that the Langmuir isotherm provided the best fit to the experimental data, yielding the highest correlation coefficients ($R^2 > 0.99$) compared with the other two models. This outcome supports the monolayer adsorption theory, suggesting that each active site on the adsorbent surface binds to a single nitrate ion [42]. The maximum adsorption capacities predicted by the Langmuir model were 39.22 mg/g for RP and 54.94 mg/g for MP. The Langmuir constant ( $K_L$ ) values were 0.072 L/mg for RP and 0.122 L/mg for MP, indicating relatively weak interactions between nitrate ions and the adsorbent surface. This implies that physical forces are likely the dominant mechanism governing the adsorption process [52]. Furthermore, the dimensionless separation factor ( $R_L$ ) values ranged from 0.355 to 0.044 for RP and 0.240 to 0.026 for MP. Since all $R_L$ values fell between 0 and 1, the adsorption of nitrate onto both adsorbents can be considered favorable.

**Table 4** Isotherm parameters of nitrate adsorption onto RP and MP.

| Isotherm models | Adsorbents | |
|---|---|---|
| | **RP** | **MP** |
| **Langmuir isotherm** | | |
| $q_{max}$ (mg/g) | 39.22 | 54.94 |
| $K_L$ (L/mg) | 0.072 | 0.122 |
| $R_L$ | 0.355 - 0.044 | 0.240 - 0.026 |
| $R^2$ | 0.997 | 0.999 |
| **Freundlich isotherm** | | |
| $K_F$ (L/g) | 6.347 | 9.208 |
| 1/n | 0.359 | 0.975 |
| $R^2$ | 0.924 | 0.873 |
| **Dubinin-Radushkevich isotherm** | | |
| $q_o$ (mg/g) | 28.803 | 37.696 |
| E (kJ/mol) | 1.459 | 0.019 |
| $R^2$ | 0.865 | 0.813 |

For the Freundlich isotherm, the RP and MP had $K_F$ values of 6.347 and 9.208 L/g, respectively. The corresponding 1/n values were 0.359 of RP and 0.975 of MP. Since both 1/n values are less than 1, this strongly suggests that the adsorption process is favorable on both surfaces [42]. The value of *n* provides insight into the surface heterogeneity and energy distribution of active sites [53]. In this study, the *n* values of RP and MP were 2.78 and 1.03, respectively. The higher *n* value of RP indicates greater surface heterogeneity and stronger adsorption affinity [54], reflecting a broader range of binding energies driven by enhanced active sites and favorable electrostatic interactions. In contrast, the lower *n* value observed for MP implies a relatively uniform surface with limited adsorption energy variation.

The Dubinin-Radushkevich isotherm is used to distinguish the sorption mechanism: a mean sorption energy E less than 8 kJ/mol suggests physisorption, whereas an E value greater than 8 kJ/mol indicates chemisorption. The calculated mean free energy of adsorption (E) of the Dubinin-Radushkevich isotherm was 1.459 kJ/mol for RP and 0.019 for MP. These values are significantly below the 8 kJ/mol threshold, which is consistent with physical adsorption, including van der Waals forces and other weak interactions [31].

The adsorption results summarized in **Table 5** clearly demonstrate the superior performance of hydrochloric acid-modified perlite (MP), which achieved a maximum adsorption capacity of 54.95 mg/g at 30 °C. This value is significantly higher than that of raw perlite (RP, 39.22 mg/g) and other modified adsorbents reported in previous studies. The enhancement in adsorption capacity upon acid modification can be attributed to several physicochemical changes induced by hydrochloric acid treatment. While modified rice husk exhibited a higher adsorption capacity (55.55 mg/g at 20 °C), MP shows competitive performance with the added advantage of being abundant, low-cost, and locally available in Thailand. Compared to biochar-based adsorbents (e.g., corncob biochar, 34.20 mg/g), MP demonstrates a more efficient adsorption mechanism, likely due to its mineral composition and enhanced surface chemistry after acid treatment. The enhanced adsorption capacity of MP relative to RP and other adsorbents reflects the mechanistic role of acid modification. Acid treatment promotes the formation of additional oxygen-containing functional groups and modifies the pore architecture, thereby increasing the availability and accessibility of adsorption sites. These changes intensify electrostatic attraction and ion-exchange interactions with nitrate, which explains the observed improvement in adsorption efficiency and highlights its applicability in nitrate-contaminated wastewater treatment systems [20].

**Table 5** The maximum adsorption capacity (mg/g) of nitrate onto various modified adsorbents.

| Adsorbates | $q_{max}$ (mg/g) | Tem (°C) | References |
|---|---|---|---|
| $ZnCl_2$-modified coconut granular activated carbon | 14.01 | 20 | Liu [55] |
| modified rice husk | 55.55 | 20 | Katal *et al.* [56] |
| modified pine sawdust | 32.5 | 5 | Keranen *et al.* [57] |
| modified pine sawdust | 29.5 | 23 | Keranen *et al.* [57] |
| modified pine sawdust | 23.8 | 40 | Keranen *et al.* [57] |
| modified granular activated carbon | 21.51 | 25 | Mazarji *et al.* [1] |
| Surfactant-modified forms of clinoptilolite | 30.2 | room temp. | Rasuli *et al.* [58] |
| Surfactant-modified forms of pumice | 27.6 | room temp. | Rasuli *et al.* [58] |
| Sulphuric acid- corncob biochar | 34.20 | 30 | Hu *et al.* [59] |
| modified corncob biochar | 10.48 | 30 | Hu *et al.* [59] |
| modified hazelnut shells | 26.51 | 25 | Stjepanovi *et al.* [13] |
| modified corn stalk | 20.04 | 30 | Wang *et al.* [10] |

| Adsorbates | $q_{max}$ (mg/g) | Tem (°C) | References |
|---|---|---|---|
| modified perlite (Iran) | 32.63 | 20 | Baei *et al.* [4] |
| raw perlite (RP) (Thailand) | 39.22 | 30 | This work |
| HCl-modified perlite (MP) (Thailand) | 54.95 | 30 | This work |

**Effect of ionic strength on nitrate adsorption**

The ionic strength of an aqueous solution is a critical factor influencing ion adsorption at the solid-liquid interface. Its effect on nitrate removal was examined through batch experiments with varying NaCl concentrations (0, 0.001, 0.01 and 0.1 mol/L), as shown in **Figure 9**. Increasing the NaCl concentration from 0 to 0.1 mol/L decreased nitrate adsorption, with values dropping from 82.15% to 34.41% for RP and from 88.23% to 36.98% for MP, indicating that adsorption on both RP and MP was strongly influenced by ionic strength. An increase in ionic strength significantly reduces nitrate adsorption at all initial NaCl concentrations. This behavior indicates that nitrate is predominantly adsorbed through outer-sphere electrostatic interactions, which are highly sensitive to compression of the electrical double layer [60].

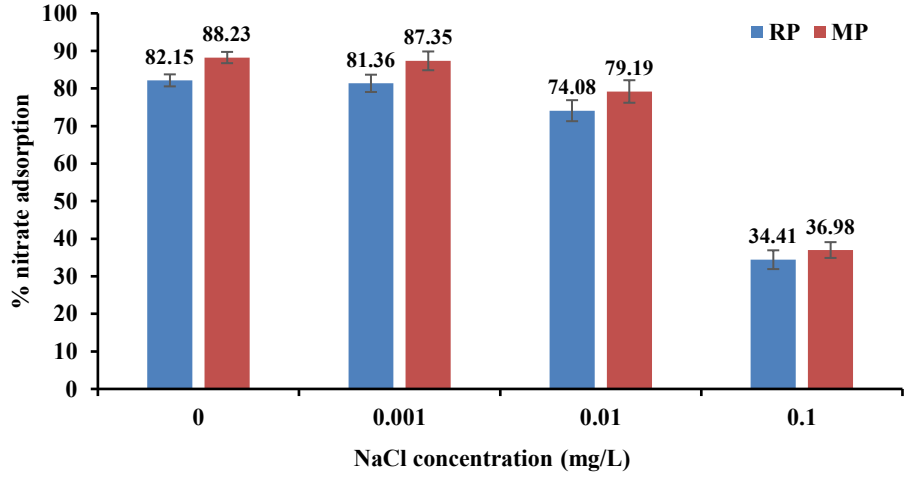


**Figure 9** Effect of NaCl ionic strength on nitrate adsorption by RP and MP; contact time 60 min, initial nitrate concentration of 50 mg/L, and adsorbent dose 0.3 g).

**Effect of coexisting anions on nitrate adsorption**

In nitrate-contaminated water, coexisting ions such as chloride, sulfate, carbonate, and phosphate (50 mg/L) competed with nitrate for adsorption sites on the adsorbents. The control condition, containing only nitrate without competing ions, is referred to as the blank, as shown in **Figure 10**. In this experiment, the concentration of each coexisting anion was adjusted to be equimolar with nitrate (i.e., a 1:1 molar ratio). Under these conditions, the relative affinity of anions followed the order phosphate > carbonate > sulfate > chloride, which is primarily governed by charge density and hydration energy. It is well established that adsorbents generally exhibit higher affinity toward anions with greater charge density and multivalent species compared to monovalent anions [61]. The presence of these anions affected nitrate removal differently across the two adsorbents. For RP, nitrate removal efficiencies were 82.26% with chloride, 65.36% with sulfate, 56.25% with carbonate, and 23.15% with phosphate. Similarly, MP exhibited efficiencies of 87.98% with chloride, 72.75% with sulfate, 60.96% with carbonate, and 27.65% with phosphate. Overall, the competitive effect followed the order phosphate > carbonate > sulfate > chloride for both adsorbents, indicating that phosphate exerted the strongest inhibitory influence. The experimental results are partially consistent with those of Chen *et al.* [43], who investigated nitrate and nitrite adsorption using magnetic Mg/Fe hydrotalcite and

reported the inhibitory effects of coexisting anions in the order phosphate > carbonate > fluoride > sulfate > chloride > chlorate. The relative affinity order of common anions has been reported as phosphate > carbonate > sulfate > chloride, consistent with previous studies on adsorption onto metal oxyhydroxides [62,63]. This order reflects the stronger binding tendency of phosphate compared to other anions, which explains its more pronounced competitive effect in multi-component groundwater systems.

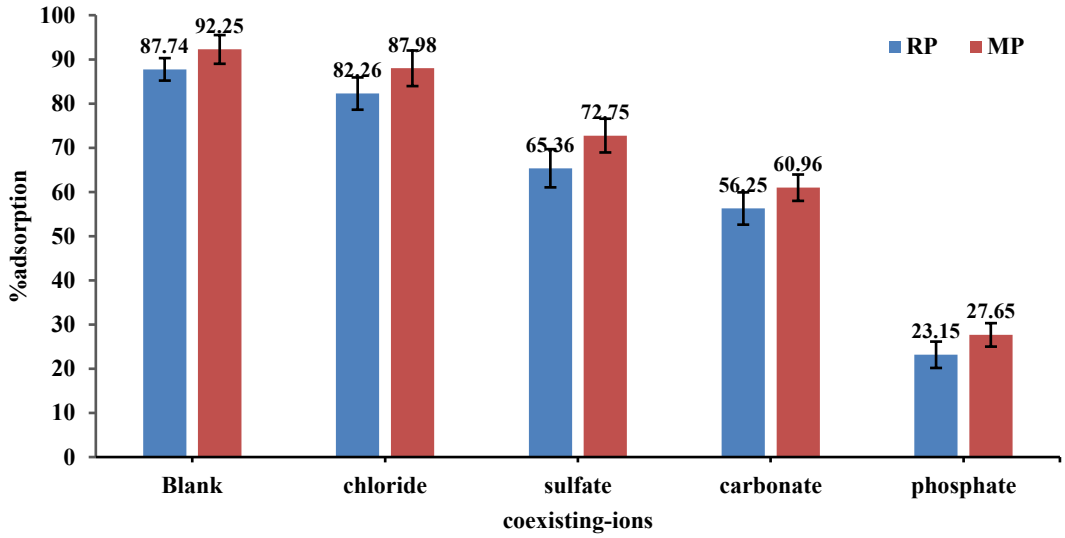


**Figure 10** Influence of coexisting anions on nitrate adsorption performance of RP and MP at a 1:1 molar ratio; pH 6, contact time 60 min, initial nitrate concentration of 50 mg/L, and adsorbent dose 0.3 g.

The adsorption mechanism of anions onto adsorbents is strongly influenced by their physico-chemical properties, including solubility, ionic radius, hydration energy, and bulk diffusion coefficient, which are crucial for selective adsorption [64]. In our study, nitrate adsorption was found to be only slightly affected by chloride ($Cl^-$), likely due to its comparable ionic radius (1.81 Å) to nitrate (1.79 Å) and its lower hydration energy, which limits its competitive interaction with adsorption sites. In contrast, sulfate ($SO_4^{2-}$) has a higher negative charge and a more pronounced influence on nitrate adsorption. Similarly, carbonate ($CO_3^{2-}$), an oxyanion with an ionic radius of 1.78 Å, was strongly adsorbed and reduced nitrate adsorption [65]. Phosphate ($PO_4^{3-}$), carrying a trivalent negative charge and higher hydration energy with an ionic radius of 2.38 Å, exhibited an exceptionally strong affinity for perlite surfaces, indicating that multivalent oxyanions compete more effectively than monovalent anions for adsorption sites and thus markedly suppress nitrate retention. According to Wang *et al.* [10], these results indicated that the affinity level between the adsorbent and adsorbate was largely determined by concentration and valence of anions.

**Thermodynamics of nitrate adsorption**

Studies on the effect of temperature on nitrate adsorption onto RP and MP were conducted at 20, 30, and 40 °C. The results revealed a positive correlation between temperature and adsorption capacity, indicating that the process is endothermic [66]. **Figure 11** illustrates the plots of the logarithm of the equilibrium constant ($Kc = q_e / C_e$) against the reciprocal of temperature (1/T). The calculated ΔG values were −2.991, −3.382, and −3.887 kJ/mol for RP, and −3.440, −3.742, and −4.199 kJ/mol for MP. The consistently negative ΔG values confirm that nitrate adsorption is thermodynamically spontaneous under the tested conditions. Moreover, the increasing negative magnitude of ΔG with rising temperature suggests that adsorption becomes more favorable at higher temperatures, likely due to the enhanced mobility of nitrate ions in solution. Typically, Gibbs free energy changes range from 80 - 400 kJ/mol for chemisorption and 0 - 20 kJ/mol for physisorption. Based on these

values, the predominant mechanism is identified as physisorption [67]. The positive enthalpy change (ΔH) values of 10.015 and 7.647 kJ/mol for RP and MP confirm that nitrate adsorption is endothermic for both adsorbents. The increase in temperature-activated adsorption sites suggests that nitrate ions require the transfer of a significant amount of heat from the aqueous solution into the solid phase [68]. The endothermic nature of the adsorption process indicates that higher temperatures provide the energy required to overcome diffusion resistance within the porous structure, supporting intraparticle diffusion as the primary rate-limiting step [69]. Similarly, the positive entropy changes (ΔS) of 44.638 and 37.758 J/mol for RP and MP, respectively, indicate greater randomness at the solid–liquid interface during adsorption. This enhanced disorder reflects the increased unpredictability associated with the adsorption process at the solid-solution interface.

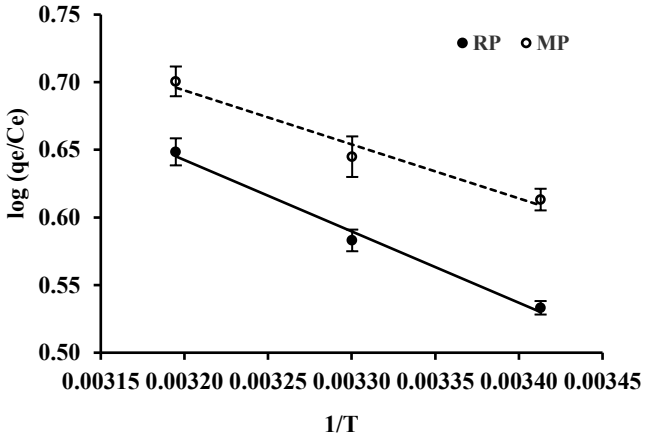


**Figure 11** Thermodynamic analysis of nitrate adsorption on RP and MP; pH 6, contact time 60 min, initial nitrate concentration 50 mg/L, and adsorbent dose 0.3 g.

**Mechanism of nitrate adsorption**

The characterization of RP and MP adsorbents, together with the nitrate adsorption results, indicated that the adsorption process involved multiple mechanisms (**Figure 12**). Adsorption was observed at pH 2, with maximum adsorption occurring at pH 6. Under these conditions, the surface of perlite became positively charged, thereby facilitating electrostatic attraction with negatively charged nitrate ions [14], as illustrated in Eq. (17). Moreover, adsorption increased with increasing solution pH, reaching a maximum at pH 6, which can be attributed to the reduction in chloride ion concentration. Consequently, the adsorption mechanism is likely governed by electrostatic competition, as illustrated in Eq. (18). The adsorption mechanism, as seen in Eq. (18), was proposed to be ligand exchange by displacement of $Cl^-$ with nitrate ions [70]. Among these, hydrogen bonding, as shown in Eq. (19), played an important role by providing additional stability during adsorption. Specifically, the hydrogen atoms in protonated hydroxyl groups interacted with the oxygen atoms of nitrate ions [44]. Evidence of hydrogen-bonding interactions was observed from slight shifts and increases in the −OH stretching vibration peaks, moving from 3,631 to 3,637 $cm^{-1}$ for RP and from 3,600 to 3,602 $cm^{-1}$ for MP.

Metal ions such as K and Fe, together with their oxides, can form hydroxides and hydrated metal oxides at the adsorbent interface [14]. Consequently, nitrate may be adsorbed through ion exchange, as illustrated in Eq. (20).

$$M/Si–OH_2^+ + NO_3^- \rightarrow M– OH_2^+ \text{----- } NO_3^- \quad (17)$$

$$M/Si–OH_2^+/Cl^- + NO_3^- \rightarrow M/Si–OH_2^+/NO_3^- + Cl^- \quad (18)$$

$$M/Si–OH + NO_3^- \rightarrow M– OH\ldots..NO_3^- \quad (19)$$

$$K/Fe–OH + NO_3^- \rightarrow K/Fe–NO_3 + OH^- \quad (20)$$

where, M represents Al, Fe, and K.

Because maximum nitrate adsorption on RP/MP was observed at pH 6, which is higher than the pHpzc, the M–OH groups become negatively charged and bind with divalent cations, thereby forming cation bridging, as illustrated in Eq. (21) [47,48].

$$Si/Al\text{–}O^{-}\cdots M^{2+} + NO_3^{-} \rightarrow Si/Al\text{–}O^{-}\cdots M^{2+}NO_3^{-} \quad (21)$$

The FTIR spectra reveal the presence of siloxane (Si–O–Si) groups from the tetrahedral sheet on the adsorbent surface, highlighting the important role of electrostatic attraction in the adsorption process. Moreover, the Si–O–Si and Al–O–Al bonds on the adsorbent surface can facilitate dipole–dipole adsorption (Van der Waals forces) with nitrate ions through intermolecular interactions [14]. The pore structures of both RP and MP further enhance the pore-filling mechanism, providing abundant adsorption sites for the effective removal of nitrate molecules.


**Figure 12** Schematic representation of the proposed mechanism for nitrate adsorption on RP and MP adsorbents.

**Batch nitrate adsorption design from equilibrium data**

Determining the appropriate amount of adsorbent required to complete the adsorption process is critical for the design of large-scale batch adsorbers. Establishing equilibrium is essential for calculating the optimal adsorbent dosage and its corresponding adsorption capacity [57]. The single-stage batch adsorption process can be evaluated using a mass balance, as expressed in Eq. (22):

$$V(C_o - C_e) = W(q_e - q_o) \quad (22)$$

since $q_o$ represents the initial capacity, it is taken as 0. According to the Langmuir isotherm, the equilibrium adsorption capacity ($q_e$) can be determined using Eq. (23):

$$q_e = \frac{q_{max} K_L C_e}{1+K_L C_e} \quad (23)$$

Substituting this expression into Eq. (20) yields Eq. (24):

$$V(C_o - C_e) = W\frac{q_{max} K_L C_e}{1+K_L C_e} \quad (24)$$

where $C_o$ (mg/L) is the initial concentration of nitrate, $C_e$ (mg/L) is the nitrate concentration at equilibrium, $q_e$(mg/g) is the equilibrium adsorption capacity, V(L) is the volume of nitrate solution, and W(g) is the mass of adsorbent.

The adsorption capacity ($q_e$) of the adsorbent was determined using the Langmuir isotherm together with the associated parameters (**Table 4**). The efficacy of the adsorbents was evaluated based on the mass required to

achieve nitrate reduction across different solution volumes. To illustrate this evaluation, **Figures 13(a)** and **13(c)** show the relationship between solution volume and adsorbent mass at a fixed concentration of 100 mg/L, whereas **Figures 11(b)** and **11(d)** depict the relationship at a fixed adsorption level of 90%.

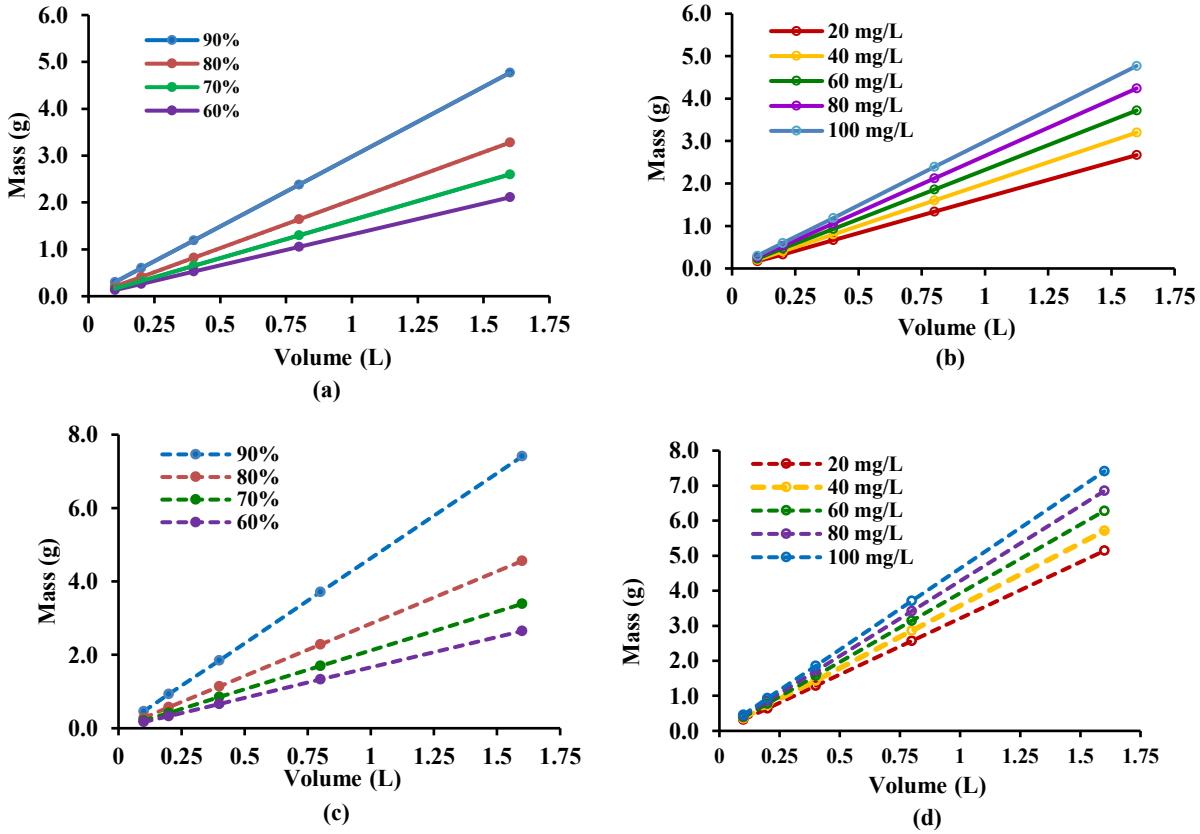


**Figure 13** Single-stage batch nitrate adsorption: (a, c) at a fixed initial nitrate concentration of 100 mg/L; (b, d) at a fixed adsorption level of 90% for RP (solid line) and MP (dotted line).

**Regeneration and reusability studies**

The practicality and cost-effectiveness of the adsorbents were evaluated through regeneration and reusability experiments for nitrate removal from water. A 0.01 M NaOH solution was used as the desorption agent. Spent adsorbents were immersed in the desorption solution for 30 min, rinsed to adjust the pH to 6 - 7, and subsequently dried for reuse in the next adsorption cycle. **Figure 14** illustrates the reusability performance of the adsorbents over five consecutive cycles. A gradual decline in adsorption efficiency was observed with each adsorption-desorption cycle. The adsorption capacity decreased progressively from the first to the fifth cycle. Specifically, nitrate removal by RP decreased from 86.52% to 45.36%, while that by MP declined from 90.80% to 50.40%.

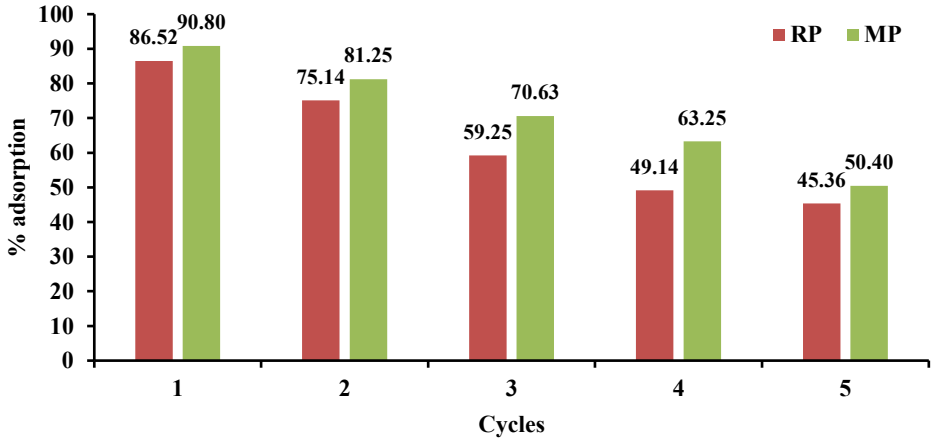


**Figure 14** Reusability performance of RP and MP in nitrate adsorption over five successive adsorption-desorption cycles.

**Nitrate adsorption in real groundwater by batch adsorption**

The batch adsorption experiments using RP and MP provide clear evidence of their effectiveness in nitrate removal from agricultural groundwater in Lopburi. At the tested condition (pH 6.25; initial nitrate concentration 49.95 mg/L; contact time 60 min), both adsorbents showed a consistent improvement in removal efficiency as the dosage increased from 0.1 to 0.3 g/100 mL. As illustrated in Figure 15, RP achieved an increase in adsorption percentage from 64.22% to 74.41%, while MP performed slightly better, rising from 71.25% to 80.63%. This trend suggests that higher adsorbent doses provide more available binding sites, thereby enhancing nitrate uptake. The comparative performance also highlights MP's relatively stronger affinity toward nitrate ions, although both materials demonstrated substantial capability in treating real agricultural groundwater. These findings reinforce the practical potential of RP and MP as viable adsorbents for mitigating nitrate contamination in field-relevant conditions.

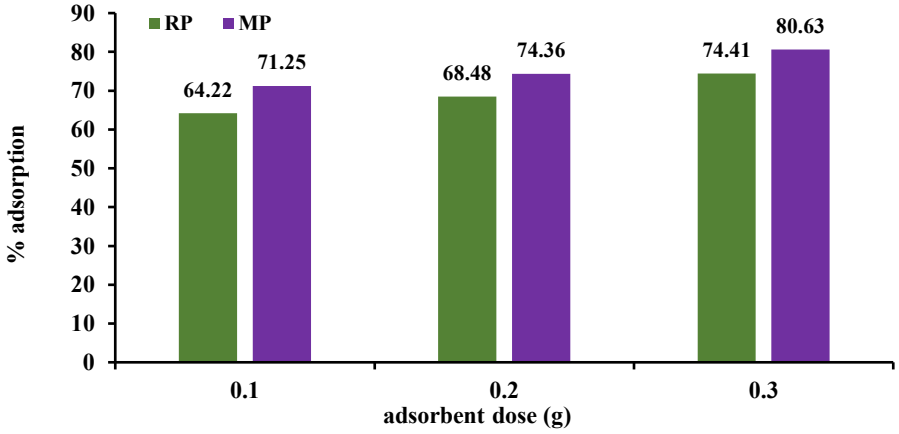


**Figure 15** Nitrate adsorption in real groundwater by RP and MP.

Although the Langmuir constant ($K_L$) values were relatively low, both RP and MP exhibited high nitrate removal efficiency in real groundwater. This apparent discrepancy can be explained by considering the Freundlich parameters. The n values of 2.78 for RP and 1.03 for MP indicate that adsorption on RP and MP is more favorable, consistent with their higher efficiency despite the low $K_L$. The lower $K_L$ may reflect weaker binding energy at individual sites, yet the heterogeneous surface and abundant adsorption sites allow effective overall uptake. Thus, the combination of the Langmuir and the Freundlich models highlights that adsorption performance in complex groundwater systems cannot be solely inferred from $K_L$, but must also account for

surface heterogeneity and the favorable adsorption behavior indicated by n.

**Cost analysis**

The utilization of naturally abundant Thai perlite for nitrate adsorption enhances local resource valorization, reduces dependence on imported adsorbents, and supports circular economy principles. This study demonstrates how a low-cost mineral precursor can be transformed into an effective adsorbent through simple acid modification, thereby improving nitrate removal efficiency. The resulting HCl-modified perlite (MP) exhibits significant economic and environmental advantages due to its straightforward preparation process and enhanced adsorption capacity. Beyond nitrate removal, the prepared MP shows potential for broader water treatment applications, particularly in rural and resource-limited communities. Additionally, its durability, reusability, and relatively low environmental footprint contribute to long-term cost effectiveness.

**Contribution to sustainable development goals and circular economy**

This research aligns with the principles of green chemistry and the circular economy, contributing directly to the United Nations Sustainable Development Goals (SDGs). By utilizing a locally abundant mineral resource (perlite) to develop an effective adsorbent for nitrate pollution, it addresses SDG 6 (Target 6.3: water quality) and SDG 12 (Targets 12.4 and 12.5: Chemicals management and resource valorization). The successful regeneration of the adsorbent over multiple cycles further reinforces this sustainable and circular approach [71,72]. Our study also responds to recent calls for SDG-oriented water treatment solutions employing low-cost, environmentally benign materials [73-75]. In addition, it contributes to the expanding body of research on biosorbents and geo-sourced materials for depollution [76-80], while highlighting the importance of evaluating sustainability and life-cycle impacts of these emerging technologies [81-83].

## Conclusions

In this study, HCl-modified volcanic rock was successfully employed for nitrate adsorption. The specific surface areas of RP and MP were found to be 23.08 and 15.69 $m^2/g$, respectively, with mesoporous structures confirmed by Type IV isotherms. Furthermore, both adsorbents were comprehensively characterized using FTIR, XRD, XRF, and SEM analyses. HCl modification effectively activated the functional groups in perlite, thereby enhancing their contribution to nitrate adsorption. Optimal removal efficiencies for RP and MP were achieved at pH 6 with an equilibrium time of 60 min. Both the pseudo-second-order kinetic model and the Langmuir isotherm exhibited an excellent fit to the adsorption data. The maximum nitrate adsorption capacities of RP and MP were 39.22 and 54.94 mg/g, respectively. Thermodynamic and activation energy analyses confirmed that nitrate adsorption on RP and MP occurs predominantly through physisorption. Mechanistic insights revealed that physical adsorption predominated, driven mainly by electrostatic interaction, hydrogen bonding, electrostatic displacement, cation bridging, pore filling, and ion exchange. The competitive effect of coexisting ions was observed in the order: phosphate > carbonate > sulfate > chloride for both adsorbents. Furthermore, application to real wastewater treatment demonstrated favorable nitrate removal performance, confirming the practical potential of RP and MP as effective adsorbents.

**Acknowledgements**

The authors would like to thank Thepsatri Rajabhat University, Thailand for the financial support.

**Declaration of Generative AI in Scientific Writing**

We have used QuillBot and Grammarly for checking the grammar and paraphrasing the written sentences.

**CRediT Author Statement**

**Suchada Sawasdee:** Conceptualization, Methodology, Formal analysis, Data Curation, Writing - Original Draft, Visualization, Project Administration. **Prachart Watcharabundit:** Writing - Review & Editing, Visualization.

**References**


[1] M Mazarji, B Aminzadeh, M Baghdadi and A Bhatnagar. Removal of nitrate from aqueous solution using modified granular activated carbon. *Journal of Molecular Liquids* 2017; **233**, 139-148.

[2] Y Liu, X Zhang and J Wang. A critical review of various adsorbents for selective removal of nitrate from water: Structure, performance and mechanism. *Chemosphere* 2022; **291**, 132728.

[3] OO Elemile, BO Akpor, EM Ibitogbe, YT Afolabi and DO Ajani. Adsorption isotherm and kinetics for the removal of nitrate from wastewater using chicken feather fiber. *Cogent Engineering* 2022; **9(1)**, 2043227.

[4] MS Baei, H Esfandian and AA Nesheli. Removal of nitrate from aqueous solutions in batch systems using activated perlite: An application of response surface methodology. *Asia-Pacific Journal of Chemical Engineering* 2016; **11(3)**, 437-447.

[5] Z Hussain, T Cheng, M Irshad, RA Khattak, C Yao, D Song and M Mohluddin. Bentonite clay with different nitrogen sources can effectively reduce nitrate leaching from sandy soil. *PLoS One* 2022; **17(12)**, e0278824.

[6] A Nemati, A Khani and M Mirzaei. Modeling of Nitrite adsorption on granular activated carbon using artificial neural network. *In*: Proceedings of the Second International Conference on Environmental and Computer Science, Dubai, United Arab Emirates. 2009, p. 118-121.

[7] Q Yin, H Ren, R Wang and Z Zhao. Evaluation of nitrate and phosphate adsorption on Al-modified biochar: Influence of Al content. *Science of the Total Environment* 2018; **(631-632)**, 895-903.

[8] M Chabani, A Amrane and A Bensmaili. Kinetic modelling of the adsorption of nitrates by ion exchange resin. *Chemical Engineering Journal* 2006; **125**, 111-117.

[9] S Singh, AG Anil, V Kumar, D Kapoor, S Subramanian, J Singh and PC Ramamurthy. Nitrates in the environment: A critical review of their distribution, sensing techniques, ecological effects, and remediation. *Chemosphere* 2022; **287**, 131996.

[10] L Wang, Z Xu, Y Fu, Y Chen, Z Pan, R Wang and Z Tan. Comparative analysis on adsorption properties and mechanisms of nitrate and phosphate by modified corn stalks. *RSC Advances* 2018; **8**, 36468-36476

[11] A Bhatnagar and M Sillanpää. A review of emerging adsorbents for nitrate removal from water. *Chemical Engineering Journal* 2011; **168**, 493-504.

[12] Z Hussain, T Cheng, M Irshad, RA Khattak, C Yao, D Song and M Mohluddin. Bentonite clay with different nitrogen sources can effectively reduce nitrate leaching from sandy soil. *PLoS One* 2022; **17(12)**, e0278824.

[13] M Stjepanovic, N Velic and M Habuda-Stanic. Modified hazelnut shells as a novel adsorbent for the removal of nitrate from wastewater. *Water* 2022; **14**, 816.

[14] L Yang, M Yang, P Xu, X Zhao, H Bai and H Li. Characteristics of nitrate removal from aqueous solution by modified steel slag. *Water* 2017; **9(10)**, 757.

[15] L Jia, B Jiang, F Huang and X Hu. Adsorption and mechanism of nitrate from groundwater onto Si–Al porous clay mineral material as ceramic waste: Characterization, kinetics, and adsorption isotherms. *Desalination and Water Treatment* 2020; **202**, 251-263.

[16] L Meesuk and S Seammai. The use of perlite to remove dark colour from repeatedly used palm oil. *ScienceAsia* 2010; **36**, 33-39.

[17] Z Khoshraftar, H Masoumi and A Ghaemi. On the performance of perlite as a mineral adsorbent for heavy metals ions and dye removal from industrial wastewater: A review of the state of the art. *Case Studies in Chemical and Environmental Engineering* 2023; **8**, 100385.

[18] M Malakootian, N Jaafarzadeh and H Hossaini. Efficiency of perlite as a low-cost adsorbent applied to the removal of Pb and Cd from paint industry effluent. *Desalination and Water Treatment* 2011; **26**, 243-249.

[19] U Selengil and D Yıldız. Investigation of the methylene blue adsorption onto waste perlite. *Desalination and Water Treatment* 2022; **262**, 235-247.

[20] P Loganathan, S Vigneswaran and J Kandasamy. Enhanced removal of nitrate from water using surface modification of adsorbents: A

review. *Journal of Environmental Management* 2013; **131**, 363-374.

[21] JM Angosto, JM Obón, MJ Roca, M Alacid and JA Fernández-López. A promising, highly effective nitrate sorbent derived from solid olive mill residues. *Agronomy* 2023; **13(5)**, 1325.

[22] S Ramalingam and A Subramania. Effective removal of nitrates from the drinking water by chemical and electrochemical methods. *Engineered Science* 2021; **15(11)**, 80-88.

[23] VP Dinh, TDT Huynh, HM Le, VD Nguyen, VA Dao, NQ Hung, LA Tuyen, S Lee, Y Junsin, TD Nguyen and LV Tan. Insight into the adsorption mechanisms of methylene blue and chromium (III) from aqueous solution onto pomelo fruit peel. *RSC Advances* 2019; **9(44)**, 25847-25860.

[24] NF Al-Harby, EF Albahly and NA Mohamed. Kinetics, isotherm and thermodynamic studies for efficient adsorption of Congo Red dye from aqueous solution onto novel cyanoguanidine-modified chitosan adsorbent. *Polymers* 2021; **13(24)**, 4446.

[25] Y Zhu, B Yi, Q Yuan, Y Wu, M Wang and S Yan. Removal of methylene blue from aqueous solution by cattle manure derived low-temperature biochar. *RSC Advances* 2018; **8**, 19917-19929.

[26] AM Alotaibi and AF Ismail. Modification of clinoptilolite as a robust adsorbent for highly-efficient removal of thorium (IV) from aqueous solutions. *International Journal of Environmental Research and Public Health* 2022; **19(21)**, 13774.

[27] JA Alexander, MAA Zaini, S Abdulsalam, UA El-Nafaty and UO Aroke. Physicochemical characteristics of surface modified Dijah-Monkin bentonite. *Particulate Science and Technology* 2018; **36(3)**, 287-297.

[28] BA Şenel, N Ateş and SS Bekaroğlu. Evaluation of characterization and adsorption kinetics of natural organic matter onto nitric acid modified activated carbon. *Environmental Research and Technology* 2024; **7(2)**, 201-211.

[29] S İnan, VV Kusumkar, M Galamboš, E Viglašová, O Rosskopfová and M Daňo. Isotherm, kinetic, and selectivity studies for the removal of 133Ba and 137Cs from aqueous solution using Turkish Perlite. *Materials* 2022; **15(21)**, 7816.

[30] P Somkiattiyot, A Wongrueng, P Induvesa, N Yodsin, S Phuphisith, P Sittisom, P Rakruam, W Srisom, P Gavila, S Chamnanprai and S Takizawa. Enhanced fluoride removal from groundwater using napier grass-derived adsorbent: experimental and DFT study. *Trends in Sciences* 2025; **22(2)**, 9217.

[31] M Saidi, BA Reguig, M El Amine Monir, TM Althagafi, M Fatmi, A Remil, A Zehhaf and MA Ghebouli. Kinetics thermodynamics and adsorption study of raw treated diatomite as a sustainable adsorbent for crystal violet dye. *Scientific Reports* 2025; **15(1)**, 21991.

[32] EG Söğüt, E Ergan, NC Kılıç, H Dönmez and E Akbaş. Methylene blue adsorption from aqueous solution by functionalized perlites: An experimental and computational chemistry study. *Desalination and Water Treatment* 2021; **217**, 391-410.

[33] O Uygun, R Güven and GÖ Çakal. Adsorptive removal of stable and radioactive Pb (II) isotopes from aqueous solution using bentonite, zeolite and perlite: Characterization, isotherm and thermodynamic studies. *Clay Minerals* 2023; **58(2)**, 195-209.

[34] Ö Aksoy, F Alyamaç, M Mocan, M Sütçü, N Özveren-Uçar and MÖ Seydibeyoğlu. Characterization of perlite powders from Izmir, Türkiye region. *Physicochemical Problems of Mineral Processing* 2022; **58(6)**, 155277.

[35] Q Yin, H Ren, R Wang and Z Zhao. Evaluation of nitrate and phosphate adsorption on Al-modified biochar: Influence of Al content. *Science of the Total Environment* 2018; **(631-632)**, 895-903.

[36] N Öztürk and TE Bektaş. Nitrate removal from aqueous solution by adsorption onto various materials. *Journal of Hazardous Materials* 2004; **112(1-2)**, 155-162.

[37] PT Phan, TT Nguyen, NH Nguyen and S Padungthon. A simple method for synthesis of triamine-$SiO_2$ material toward aqueous nitrate adsorption. *Environment and Natural Resources Journal* 2019; **17(4)**, 59-67.

[38] A Bhatnagar and M Sillanpää. A review of emerging adsorbents for nitrate removal from water. *Chemical Engineering Journal 2011*; **168**, 493-504.

[39] M Khatamian, SK Derakhshan, SH Nami and S Fazli-Shokouhi. Nitrate removal study of synthesized nano γ-alumina and magnetite-alumina nanocomposite adsorbents prepared by various methods and precursors. *Scientific Reports* 2024; **14(1)**, 7673.

[40] L Jiang, H Yu, L Pei and X Hou. The effect of temperature on the synergistic effect between a magnetic field and functionalized graphene oxide carbon nanotube composite for $Pb^{2+}$ and phenol adsorption. *Journal of Nanomaterials* 2018; **2018**, 9167938.

[41] BD Chalageri, RM Kulkarni and A Narula. Nitrate removal from aqueous solution using fuller's earth and modified fuller's earth. *International Journal of Sustainable Engineering* 2024; **17(1)**, 601-612.

[42] D He, J Zhang, Z Shang and C Zhang. Adsorption of Ni $^{2+}$ on malic acid modified activated carbon from *Phragmites australis*. *ScienceAsia* 2022; **48(5)**, 588-595.

[43] J Chen, Y Wei, H Ji, P Guo, D Wan, B Li and X Sun. Adsorption of nitrate and nitrite from aqueous solution by magnetic Mg/Fe hydrotalcite. *Water Supply* 2021; **21(8)**, 4287-4300

[44] T Li, L Liu, M Li and Y Li. Enhanced nitrate removal from aqueous solutions using amine-functionalized biowaste-derived adsorbent. *Scientific Reports* 2025; **15(1)**, 36534.

[45] Q Shi, S Zhang, M Xie, C Christodoulatos and X Meng. Competitive adsorption of nitrate, phosphate, and sulphate on amine modified wheat straw: *In-situ* infrared spectroscopic and density functional theory study. *Environmental Research* 2022; **215**, 114368.

[46] S Zhu, P Zhang, Y Liang, M Wang, J Xiong and W Tan. Effects of aluminum substitution on the surface charge of colloidal goethite particles: Experiments and MUSIC modeling. *Environmental Science and Pollution Research* 2020; **27**, 38397-38406.

[47] X Wang, SY Lee, K Miller, R Welbourn, I Stocker, S Clarke, M Casford, P Gutfreund and MWA Skoda. Cation bridging studied by specular neutron reflection. *Langmuir* 2013; **29**, 5520-5527.

[48] J Gerold and C Henry. Observation of dynamic surfactant adsorption facilitated by divalent cation bridging. *Langmuir* 2018; **34(7)**, 2105-2114.

[49] KM Wagner, T Karathanasis and CJ Matocha. Reactivity of nitrate with zero-valent iron. *Water* 2022; **14**, 2796.

[50] B Mehdinejadiani, SM Amininasab and L Manhooei. Enhanced adsorption of nitrate from water by modified wheat straw: Equilibrium, kinetic and thermodynamic studies. *Water Science and Technology* 2019; **79(2)**, 302-313.

[51] M Stjepanović, N Velić and M Habuda-Stanić. Modified grape seeds: A promising alternative for nitrate removal from water. *Materials* 2021; **14(17)**, 4791.

[52] J Raoof and G Nahid. Evaluating the efficiency of two-parameter adsorption isotherm models in the adsorption of methylene blue. *Iranian Journal of Chemistry and Chemical Engineering* 2024; **43**, 1533-1549.

[53] A Acharya, G Jeppu, B Prabhu, CR Girish, VR Murty, AS Martis and S Ramesh. Adsorption of arsenic and fluoride: Modeling of single and competitive adsorption systems. *Helion* 2024; **10**, e31967.

[54] EM Garcia, HA Taroco and JOF Melo. Highly efficient *Eugenia dysenterica* DC seeds biomass as adsorbent for methylene blue removal. *Discover Chemistry* 2025; **2**, 11.

[55] L Liu, M Ji and F Wang. Adsorption of nitrate onto $ZnCl_2$-modified coconut granular activated carbon: Kinetics, characteristics, and adsorption dynamics. *Advances in Materials Science and Engineering* 2018; **2018**, 1939032.

[56] R Katal, MS Baei, HT Rahmati and H Esfandian. Kinetic, isotherm and thermodynamic study of nitrate adsorption from aqueous solution using modified rice husk. *Journal of Industrial and Engineering Chemistry* 2012; **18**, 295-302.

[57] A Keränen, T Leiviskä, O Hormi and J Tanskanen. Removal of nitrate by modified pine sawdust: Effects of temperature and co-existing anions. *Journal of Environmental Management* 2015; **147**, 46-54.

[58] L Rasuli, S Nasseri and M Hadi. Performance of surfactant-modified forms of clinoptilolite and pumice in nitrate removal from aqueous

solution. *Desalination and Water Treatment* 2020; **180**, 227-236.

[59] X Hu, Y Xue, L Long and K Zhang. Characteristics and batch experiments of acid-and alkali-modified corncob biomass for nitrate removal from aqueous solution. *Environmental Science and Pollution Research* 2018; **25(20)**, 19932-19940.

[60] L Wang, S Liu, W Xuan, S Li and A Wei. Efficient nitrate adsorption from groundwater by Biochar-Supported Al-Substituted goethite. *Sustainability* 2022; **14**, 7824.

[61] LV Constantino, JN Quirino, AM Monteiro, T Abrao, PS Parreira, A Urbano and MJ Santos. Sorption-desorption of selenite and selenate on Mg-Al layered double hydroxide in competition with nitrate, sulphate, and phosphate. *Chemosphere* 2017; **181**, 627-634.

[62] SI Pechenyuk, YP Semushina and LF Kuz'Mich. Adsorption affinity of anions on metal oxyhydroxides. *Russian Journal of Physical Chemistry A* 2013; **87(3)**, 490-496.

[63] A Villabona-Ortiz, R Ortega-Toro and C Tejada-Tovar. Selective and competitive adsorption of anions in solution on porous adsorbent from *Zea mays* steams: Kinetic and equilibrium study. *Water* 2022; **14**, 2906.

[64] R Nabizadeh, M Jahangiri-Rad and S Sadjadi. Modelling the effects of competing anions on fluoride removal by functionalized polyacrylonitrile coated with iron oxide nanoparticles. *South African Journal of Chemistry* 2015; **68**, 201-207.

[65] HAT Banu, P Karthikeyan and S Meenakshi. Removal of nitrate and phosphate ions from aqueous solution using zirconium encapsulated chitosan quaternized beads: Preparation, characterization and mechanistic performance. *Results in Surfaces and Interfaces* 2021; **3**, 100010.

[66] LD Hafshejani, A Hooshmanda, AA Naseri, AS Mohammadi, F Abbasi and A Bhatnagar. Removal of nitrate from aqueous solution by modified sugarcane bagasse biochar. *Ecological Engineering* 2016; **95**, 101-111.

[67] D Sateu and T Malutan. Industrial cellolignin wastes as adsorbent for removal of methylene blue dye from aqueous solutions. *BioResource* 2013; **8(1)**, 427-446.

[68] AR Kul and H Koyuncu. Adsorption of Pb(II) ions from aqueous solution by native and activated bentonite: Kinetic, equilibrium and thermodynamic study. *Journal of Hazardous Materials* 2010; **179**, 332-339.

[69] R Mohammadi, G Eshaq, MKH Winkler and A Pihlajamaki. Magnetic biochar aluminum cross-linked composite beads for preferential phosphate separation from phosphate-rich effluents. *Journal of Environmental Chemical Engineering* 2025; **13**, 116815

[70] Z Ren, X Xu, X Wang, B Gao, Q Yue, W Song, L Zhang and H Wang. FTIR, Raman, and XPS analysis during phosphate, nitrate and Cr (VI) removal by amine cross-linking biosorbent. *Journal of Colloid and Interface Science* 2016; **468**, 313-323.

[71] A Chahid, S Meftah, M Essahli, M Chafi, R Kellal, DB Left and M Zertoubi. Eco-friendly approach to corrosion inhibition of aluminum by Congo red dye in alkaline media: Experimental assessment, QSAR modeling, diffusion studies, and DFT/MC/MD simulations. *Hybrid Advances* 2025; **8**, 100532.

[72] A Chahid, M Chafi, M Essahli, AA Alrashdi and H Lgaz. Exploring the efficacy of Congo Red dye as a corrosion inhibitor for aluminum in HCl solution: An interdisciplinary study with RSM modeling and theoretical simulations. *Arabian Journal of Chemistry* 2024; **17(7)**, 105810.

[73] K Meftah, S Meftah, I Ballou, T Bouzid, S Touil and A Abid. Impact of storage conditions of *Opuntia ficus-indica* pieces on plant quality, powder composition, and extracted bioflocculant efficiency. *Environmental Science and Pollution Research* 2025; **32(47)**, 26840-26857.

[74] K Meftah, S Meftah, H Lamkhanter, S Touil and A Abid. Study of Methylene Blue dye adsorption onto biochar derived from *Austrocylindropuntia subulata* plant. *IOP Conference Series: Earth and Environmental Science* 2024; **1398**, 012006.

[75] M Drissi, S Meftah and L Skalli. The role of universities in implementing the sustainable development goals (SDGs): A case study of Hassan first university 2018-2023. *Discover Sustainability* 2025; **6**, 926.

[76] S Meftah, K Meftah, H Lamkhanter, T Mehdi, A Amahrouss, F Assadi, M Ghachi and L Bouyzza. The main types of derivatives of plant matter and agricultural waste used as bio-adsorbents for the removal of heavy metals and dyes: A review. *Egyptian Journal of Chemistry* 2024; **67(9)**, 185-207.

[77] K Meftah, S Meftah, H Lamkhanter, T Bouzid, Y Rezzak, S Touil and A Abid. Extraction and optimization of *Austrocylindropuntia subulata* powder as a novel green coagulant. *Desalination and Water Treatment* 2024; **318**, 100339.

[78] K Meftah, S Meftah, H Lamkhanter, I Hamzaoui, S Touil and A Abid. Green flocculant performance for wastewater treatment using cactus plant powder: A mini-review. *Journal of Analytical Sciences and Applied Biotechnology* 2023; **5(1)**, 29-34.

[79] K Meftah, S Meftah, I Ballou, I Hamzaoui, J Fatihi, O Kharifi, S Touil and A Abid. Storage post-harvest of *Opuntia ficus-indica* and its impact on the efficiency of bio-coagulants/flocculants extracted. *Water and Environment Journal* 2025; **39(2)**, 245-255.

[80] K Meftah, S Meftah, I Ballou, T Bouzid, S Touil and A Abid. Impact of storage conditions of *Opuntia ficus-indica* pieces on plant quality, powder composition, and extracted bioflocculant efficiency. *Environmental Science and Pollution Research* 2025; **32(47)**, 26840-26857.

[81] S Meftah, K Meftah, M Drissi, I Radah, K Malous, A Amahrous, S Touil and L Bouyazza. Heavy metal polluted water: Effects and sustainable treatment solutions using bio-adsorbents aligned with the SDGs. *Discover Sustainability* 2025; **6(1)**, 137.

[82] S Meftah, K Meftah, N Babassa, K Malous, M Drissi, A Amahrous, S Touil and L Bouyzza. The versatility and effectiveness of bio-adsorbents in the removal of chemical pollutants from water: Adsorption mechanisms, optimization by ANN and RSM, SWOT analysis, and contribution to the 3rd and 6th Sustainable Development Goals. *Discover Sustainability* 2025; **6(1)**, 971.

[83] A Chahid, M Mouloudi, S Meftah, M Essahli, M Chafi and A Ech-chahad. A multi-scale investigation of the anti-corrosion and diffusion properties of a natural dye extract on aluminum in NaCl solution using: DFT, RDF, FFV, and MC/MD simulations. *Scientific African* 2025; **27**, e03063.